

DRAFT VERSION OCTOBER 28, 2021
 Typeset using L^AT_EX **modern** style in AASTeX63

Small Planet Sizes Evolve Over Billions of Years

TREVOR J. DAVID ,^{1, 2} GABRIELLA CONTARDO ,¹ ANGELI SANDOVAL ,³
 RUTH ANGUS ,^{2, 1, 4} YUXI (LUCY) LU ,^{4, 2} MEGAN BEDELL ,¹
 JASON L. CURTIS ,² DANIEL FOREMAN-MACKEY ,¹ BENJAMIN J. FULTON ,^{5, 6}
 SAMUEL K. GRUNBLATT ,^{2, 1} AND ERIK A. PETIGURA ,⁷

¹*Center for Computational Astrophysics, Flatiron Institute, New York, NY 10010, USA*

²*American Museum of Natural History, Central Park West, New York, NY 10024, USA*

³*Department of Physics and Astronomy, Hunter College, City University of New York, New York, NY 10065, USA*

⁴*Department of Astronomy, Columbia University, 550 West 120th Street, New York, NY, USA*

⁵*California Institute of Technology, Pasadena, CA 91125, USA*

⁶*IPAC-NASA Exoplanet Science Institute Pasadena, CA 91125, USA*

⁷*Department of Physics and Astronomy, University of California, Los Angeles, CA 90095, USA*

(Received October 28, 2021)

Submitted to AAS Journals

ABSTRACT

The radius valley, a bifurcation in the size distribution of close-in *Kepler* planets, is hypothesized to be a signature of planetary atmospheric loss. Such an evolutionary phenomenon should depend on the age of the star-planet system. In this work, we study the temporal evolution of the radius valley using two independent determinations of host star ages among the California–*Kepler* Survey (CKS) sample. We find evidence for a wide and nearly empty void of planets in the period-radius diagram at the youngest system ages (\lesssim 2–3 Gyr) represented in the CKS sample. At older system ages, the radius valley appears progressively more filled in. We show that the orbital period dependence of the radius valley among the younger CKS planets is consistent with that found among those planets with asteroseismically determined host star radii. While the slopes are consistent, the radius valley determined among the younger planetary sample is shifted to smaller radii, compatible with an atmospheric loss timescale on the order of gigayears for the largest and most massive planetary cores. Our results suggest that the radius valley may be a transient feature in the radius distribution of exoplanets, being weaker among older planet populations.

Corresponding author: Trevor J. David
 ttdavid@flatironinstitute.org

Keywords: Exoplanets (498) — Exoplanet evolution (491) — Exoplanet astronomy (486) — Super Earths (1655) — Mini Neptunes (1063)

1. INTRODUCTION

By far the most intrinsically common planets known are *Kepler* planets; named for NASA’s *Kepler* mission (Borucki et al. 2010) which revealed their surprising abundance, these planets have sizes $<4 R_{\oplus}$ and separations <1 au. Some 30–60% of Sun-like stars host a *Kepler* planet, depending on assumptions about the intrinsic multiplicity and inclination dispersion within planetary systems (Fressin et al. 2013; Petigura et al. 2013; Zhu et al. 2018). An enduring mystery posed by *Kepler* planets is how some accreted sizable atmospheres while others appear to have avoided runaway accretion altogether (e.g. Lee et al. 2014; Lee & Chiang 2016). Often times *Kepler* multiplanet systems host both planets with and without atmospheres, in some cases separated from one another by only a hundredth of an astronomical unit (Carter et al. 2012).

Recent progress in understanding *Kepler* planets has been fueled by improved precision in stellar and planetary parameters. Through homogeneous spectroscopic characterization of >1300 *Kepler* planet hosts the California–*Kepler* Survey (hereafter CKS, Petigura et al. 2017; Johnson et al. 2017) revealed that the size distribution of close-in ($P < 100$ days) *Kepler* planets is bimodal, with a valley in the completeness-corrected radius distribution between 1.5 and 2 Earth radii (Fulton et al. 2017). The radius valley is widely believed to be a signature of atmospheric loss. This belief is bolstered by determinations of planet densities on either side of the valley: planets below the valley, dubbed super-Earths, have densities consistent with a rocky composition, while planets above the valley, known as sub-Neptunes, require atmospheres of a few percent by mass to explain the low measured densities (e.g. Weiss & Marcy 2014; Rogers 2015). In the atmospheric loss model some fraction of super-Earths are the remnant cores of planets that shed their primordial envelopes, which potentially alleviates the issue of neighboring planets with dissimilar densities (e.g. Lopez & Fortney 2013; Owen & Morton 2016).

Atmospheric loss requires energy. Energy deposited into a planet’s atmosphere, from an internal or external source, can heat gas to velocities exceeding the planet’s escape velocity. External mechanisms of energy deposition include photoevaporation (heating of the planet’s thermosphere by X-ray and extreme ultraviolet radiation, e.g. Owen & Jackson 2012) and impacts by planetesimals or planetary embryos (Liu et al. 2015; Inamdar & Schlichting 2016; Chatterjee & Chen 2018; Wyatt et al. 2020). Internal energy deposition can be provided by the luminosity of a planet’s cooling core (e.g. Ginzburg et al. 2016). Notably, planetary evolution models studying the effect of photoevaporation predicted the existence of a radius valley before it was observed (Owen & Wu 2013; Lopez & Fortney 2013; Jin et al. 2014; Chen & Rogers 2016).

However, subsequent studies considering the effects of core-powered mass loss were also able to reproduce the bimodal radius distribution of *Kepler* planets (Ginzburg et al. 2018; Gupta & Schlichting 2019, 2020). Photoevaporation and core-cooling remain the two leading explanations for the radius valley, and both processes may well be important, but to determine the relative importance of the two effects will require a better understanding of the dependence of the valley on other key parameters.

Determining how empty the radius gap is represents an important step toward understanding its origins. In the initial CKS sample, typical planet radius uncertainties were comparable to the width of the gap so that an intrinsically empty gap would not have been resolved (Fulton et al. 2017). Van Eylen et al. (2018) studied planets orbiting a subset of *Kepler* host stars with precise asteroseismic parameters (including ages ranging from \sim 2–10 Gyr) and found a gap considerably wider and emptier than that found in the initial CKS sample. Including trigonometric parallaxes from Gaia DR2, Fulton & Petigura (2018) were able to improve the median R_* errors by a factor of five in the CKS sample but the gap remained populated. Those authors presented simulations which indicate that the gap is not empty (i.e. solely filled in by noisy data), and that there are real planets in the gap. More recently, Petigura (2020) showed that a sizable number of planets in and around the gap have poorly determined radii due to high impact parameters, indicating the gap may be emptier than previously appreciated.

It also appears that the gap, which is a one-dimensional projection of a higher dimensional manifold, is partially filled in due to a dependence of the gap center on orbital period (or stellar light intensity) and host star mass. The gap center is anti-correlated with orbital period (Fulton et al. 2017; Van Eylen et al. 2018; Martinez et al. 2019), which is considered compatible with both the photoevaporation (e.g. Owen & Wu 2013, 2017; Lopez & Rice 2018; Jin & Mordasini 2018) and core-powered mass-loss models (e.g. Gupta & Schlichting 2019, 2020), but incompatible with formation in a gas-poor disk (Lopez & Rice 2018); at larger orbital periods, only the smallest and least massive cores are susceptible to total atmospheric loss, driving the gap to smaller radii. The length of the radius valley, i.e. its outer boundary in either period or insolation, may also provide clues to its origin, though this parameter remains poorly studied. In the photoevaporation model, the radius valley should not extend beyond orbital periods of 30–60 days as the incident XUV flux is believed to be too low to drive substantial mass loss (Owen & Wu 2017). However, the low completeness of the *Kepler* data set for small planets at these orbital periods presents a challenge for detecting such a transition point.

The gap center is positively correlated with stellar mass (Fulton & Petigura 2018; Wu 2019; Cloutier & Menou 2020; Berger et al. 2020a; Hansen et al. 2020). This observation has been used to argue support for photoevaporation (e.g. Wu 2019), but requires that the average planet mass scales approximately linearly with host star mass, an assertion that has not been verified for *Kepler* planets. By comparison, in

the core-powered mass-loss model the dependence of the radius gap location on stellar mass is a natural consequence of the dependence of planet equilibrium temperature (which partially determines the mass-loss rate in the Bondi-limited regime) on the stellar mass-luminosity relation (e.g. [Gupta & Schlichting 2020](#)).

As for metallicity, there is tentative evidence for a wider radius valley for metal-rich stars ([Owen & Murray-Clay 2018](#)). Such a dependence could result if the core mass distributions, core bulk densities, or initial atmospheric mass fractions of *Kepler* planets depend sensitively on the metallicity of the host star, and hence protoplanetary disk. There is evidence that large *Kepler* planets ($2\text{--}8 R_\oplus$) are more common around higher metallicity stars ([Dong et al. 2018](#); [Petigura et al. 2018](#)) and that planets at short orbital periods are preferentially larger around higher metallicity stars ([Owen & Murray-Clay 2018](#)). Both findings are compatible with a scenario in which metal-rich stars form more massive cores, on average. It has also been suggested that metal-rich stars host planets with higher atmospheric metallicities, which increases the efficiency of atomic line cooling in photoevaporative flows and decreases mass-loss rates ([Owen & Murray-Clay 2018](#)). In the core-powered mass-loss model, the rate at which sub-Neptunes cool and contract is anti-correlated with the opacity of the envelope, which is assumed to be proportional to the stellar metallicity ([Gupta & Schlichting 2020](#)). Thus, in both the photoevaporation and core-cooling models, larger sub-Neptunes and a consequently wider radius valley are expected around more metal-rich stars (for fixed mass and age, and neglecting any potential scaling between metallicity and core mass distributions).

The characteristic timescale for atmospheric loss among close-in exoplanets has been proposed as a key parameter for assessing the relative importance of photoevaporation and core-powered mass loss. Firm observational constraints on that timescale, however, are lacking. Constraining this timescale through exoplanet population studies may provide a means for discerning the relative importance of proposed mass loss mechanisms. Core-powered mass loss is believed to operate over gigayear timescales ([Ginzburg et al. 2016, 2018](#); [Gupta & Schlichting 2019, 2020](#)). By comparison, photoevaporation models predict the majority of mass-loss to occur during the first 0.1 Gyr (e.g. [Lopez et al. 2012](#); [Lopez & Fortney 2013](#); [Owen & Jackson 2012](#); [Owen & Wu 2013, 2017](#)), corresponding roughly to the length of time a Sun-like star spends as a saturated X-ray emitter (e.g. [Jackson et al. 2012](#); [Tu et al. 2015](#)). However, a more recent study found that the majority of the combined X-ray and extreme UV emission of stars occurs after the saturated phase of high energy emission, implying that XUV irradiation of exoplanet atmospheres continues to be important over gigayear timescales ([King & Wheatley 2020](#)). If valid, then observational constraints on exoplanet evolution timescales may not provide a conclusive metric for discerning the relative importance of photoevaporation and core-powered mass-loss.

A basic prediction of atmospheric loss models is that the radius gap is wider at younger ages and fills in over time; at a fixed value of high energy incident flux

and initial atmospheric mass fraction, photoevaporation models predict that sub-Neptunes with the least massive cores (and smallest core sizes) will cross the gap first, with more massive cores crossing the gap at later times, if at all. As a result, the radius valley is expected to be wider and emptier at early times, progressively filling in with stripped cores of ever larger masses and sizes (e.g. [Rogers & Owen 2020](#)). In the core-powered mass-loss model, [Gupta & Schlichting \(2020\)](#) suggest the average size of sub-Neptunes is expected to decline with age while the average size of super-Earths remains relatively constant, again leading to a wider and emptier radius valley at earlier times.

While the specific theoretical predictions for the age dependence of the radius valley morphology are uncertain, the fundamental prediction from atmospheric loss models that this feature should weaken with increasing age is a firm conclusion. We aim to investigate this hypothesis using the CKS sample. Here we investigate the time evolution of the exoplanet radius gap. In §2 we describe our sample selection process, including several filters intended to rid our sample of stars or planets with unreliable parameters. Our analysis procedures are discussed in §3, and finally we interpret our results and summarize our primary findings in §4.

2. SAMPLE SELECTION

We began with the CKS VII sample published in [Fulton & Petigura \(2018\)](#), hereafter F18. The CKS VII sample is a well-characterized subset of all *Kepler* planet candidates. Stellar characterization for these stars was performed in a homogeneous manner, with spectroscopic T_{eff} , $\log g$, and [Fe/H] derived from high signal-to-noise, high-dispersion Keck/HIRES spectra ([Petigura et al. 2017](#); [Johnson et al. 2017](#)). F18 derived stellar radii from the Stefan-Boltzmann law using their spectroscopic T_{eff} and bolometric luminosities computed from *Gaia* DR2 parallaxes ([Gaia Collaboration et al. 2018](#)), extinction-corrected 2MASS K_s magnitudes ([Cutri et al. 2003](#)), and theoretical bolometric corrections from the MESA Isochrones and Stellar Tracks (MIST, [Choi et al. 2016](#); [Dotter 2016](#)). F18 additionally computed ages for the CKS sample using the `isoclassify` package ([Huber et al. 2017](#)), which also depends on the MIST models. We use the F18 median posterior isochrone ages as one source of age in the analysis that follows.

We constructed several filters, many motivated by the cuts outlined in F18, to refine the sample and select those planets and stars with the most reliable parameters. The filters are enumerated as follows:

1. *Planet orbital period.* We restricted our analysis to planets with orbital periods <100 days. At larger periods *Kepler* suffers from low completeness, particularly for small planets.
2. *Planet size.* We restricted our analysis to planets with sizes $<10 R_{\oplus}$.

3. *Planet radius precision.* We restricted our analysis to planets with fractional radius uncertainties $\sigma_{R_P}/R_P < 20\%$.
4. *Planet false positive designation.* We excluded planets identified as false positives in Table 4 of the CKS I paper (Petigura et al. 2017), which synthesized dispositions from Mullally et al. (2015), Morton et al. (2016), and the NASA Exoplanet Archive (as accessed on Feb. 1, 2017, Akeson et al. 2013).
5. *Stellar radius (dwarf stars).* We restricted our analysis to dwarf stars with the following condition:

$$\left(\frac{T_{\text{eff}} - 5500}{7000} \right) + 0.15 < \log_{10} \left(\frac{R_{\star}}{R_{\odot}} \right) < \left(\frac{T_{\text{eff}} - 5500}{4500} \right) + 0.25. \quad (1)$$

The left hand side of this condition excludes a small number of stars far below the main sequence which may have erroneous parameters. The right hand side excludes stars which have evolved considerably away from the main sequence. This cut is depicted in Figure 1. We additionally excluded cool stars elevated from the main sequence which would result in unrealistically old ages. This cut was performed by requiring $T_{\text{eff}} > T_{\text{isoc}}$ where T_{isoc} is the temperature of a $\log(\text{age}) = 10.25$, $[\text{Fe}/\text{H}] = +0.25$ MIST v1.1 non-rotating isochrone with equivalent evolutionary point (EEP) < 500 .

6. *Stellar mass.* We wish to isolate the effect of stellar age on the exoplanet radius gap, while minimizing the effects of stellar mass as much as possible. We restricted our sample to stars with masses $0.75 < M_{\star}/M_{\odot} < 1.25$, where the masses were derived from stellar evolution models in F18.
7. *Stellar metallicity.* For the same reason we confined our sample in stellar mass, we restricted our analysis to stars with spectroscopically determined metallicities in the range $-0.3 < [\text{Fe}/\text{H}] < +0.3$.
8. *Isochrone parallax.* We removed stars where the *Gaia* and F18 “spectroscopic” or “isochrone” parallaxes differed by more than 4σ , where the latter quantities were computed in Table 2 of CKS VII. F18 speculated that such discrepancies may be due to flux contamination from unresolved binaries. This cut also removes all stars where the CKS VII isochrone-derived radius, R_{iso} , differed by more than 10% from the radius derived from the Stefan-Boltzmann law.
9. *Stellar dilution (*Gaia*).* We used the r_8 column in Table 2 of CKS VII to exclude stars with closely projected sources detected by *Gaia* that contribute a non-negligible fraction of the optical flux in the *Kepler* aperture. We excluded stars where additional sources in an $8''$ radius (two *Kepler* pixels) contribute more than 10% of the cumulative *G*-band flux (including the target).

10. *Stellar dilution (Imaging).* As in F18, we excluded KOIs with closely-projected stellar companions bright enough to require corrections to the planetary radii of 5% or more. Like F18, we use the radius correction factor (RCF) computed by [Furlan et al. \(2017\)](#) based on high-resolution imaging from several authors, accepting planets for which $\text{RCF} < 1.05$.
11. *Unresolved binaries (Gaia).* We excluded stars with *Gaia* RUWE values > 1.4 , where these values were queried from the *Gaia* archive.¹ The renormalized unit weight error, or RUWE, is a goodness-of-fit metric for a single star astrometric model ([Lindegren et al. 2018](#)). RUWE is a sensitive indicator of unresolved binaries ([Belokurov et al. 2020](#)), which are a concern for planet radius studies due to potential flux dilution or misidentification of the planet host.
12. *Discrepant photometry.* We removed stars with discrepant optical brightnesses, $|G - K_P| > 1$ mag, indicating a potentially erroneous cross-match between the *Kepler* and *Gaia* sources.
13. *Reddening.* We removed stars with reddening estimates of $A_V > 0.5$ mag, where these estimates were sourced from [Lu et al. \(2020\)](#). Stars with high reddening are more susceptible to erroneously determined stellar parameters.
14. *Planets with grazing transits.* Due to degeneracies inherent to light curve modeling, planets with grazing transits can have poorly constrained radii. [Petigura \(2020\)](#) showed that there is some level of contamination of the radius valley from planets with grazing transits. Since impact parameters measured from long cadence photometry are unreliable, we follow [Petigura \(2020\)](#) and exclude planets with $R_\tau < 0.6$, where R_τ is the ratio of the measured transit duration to the duration of a $b = 0, e = 0$ transit with the same period around the same star.

The overall CKS VII sample contains 1913 planets orbiting 1189 unique stellar hosts. In the analysis that follows, we will refer to the base sample (constructed from the first five cuts enumerated) and the filtered sample (constructed from all of the filters). After applying the filters, the base sample consists of 1443 planets orbiting 871 unique stellar hosts. The filtered sample consists of 732 planets orbiting 466 unique hosts. Later, we find that our analysis is insensitive to many of these restrictions and relax most of them.

2.1. *Rotation period vetting*

We supplemented the CKS sample with stellar rotation periods, which we use in §3.2 to empirically age-rank planet hosts, compiled from the literature. In order to perform an accurate rotation-based selection it is imperative to have reliable rotation

¹ <https://gea.esac.esa.int/archive/>

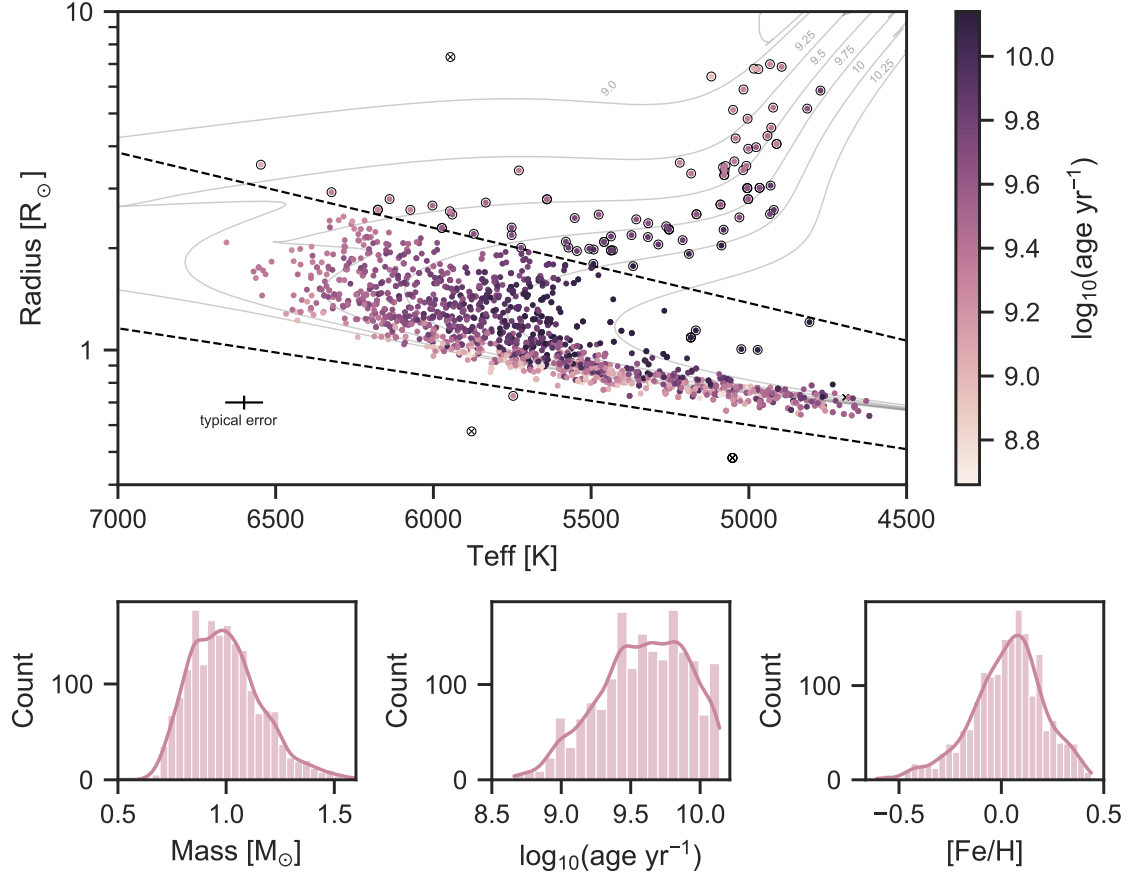


Figure 1. *Top:* H-R diagram for the CKS VII sample (Fulton & Petigura 2018). Point colors indicate median posterior ages from that work. Dashed lines indicate the dwarf star selection criteria explained in §2. Points with encircled by black rings were excluded from our analysis, and points indicated by X marks lack ages. Grey curves indicate solar-metallicity, non-rotating MIST v1.1 isochrones (Choi et al. 2016; Dotter 2016). *Bottom:* Distributions of host star masses (left), ages (middle), and metallicities (right) after performing the dwarf star cut. Note, stars hosting multiple planets are represented more than once in these distributions. All parameters originate from F18.

periods. To this end we performed visual vetting of the full *Kepler* light curves for each star in the CKS sample. For each star, our period vetting procedure consisted of the following steps:

1. Retrieve the full *Kepler* long cadence PDCSAP light curve (Stumpe et al. 2012; Smith et al. 2012) from MAST², mask known transits using ephemerides from the KOI cumulative table³, mask data with nonzero PDCSAP_QUALITY flags, and median normalize each quarter of data.

² https://archive.stsci.edu/kepler/search_retrieve.html

³ <https://exoplanetarchive.ipac.caltech.edu/docs/PurposeOfKOITable.html#cumulative>

Table 1. Rotation periods of KOIs in CKS VII sample.

KOI	KIC	P_{rot}	P_{rot}	Ref.	Flag	A18 P_{rot}	M13 P_{rot}	M15 P_{rot}	W13 P_{rot}
10	6922244	7.46		A18	2	7.46	...	82.12	...
49	9527334	8.74		A18	3	8.74	8.55	8.59	8.60
63	11554435	5.49		A18	3	5.49	5.41	...	5.39

NOTE—Flag meanings are as follows, 3: highly reliable, 2: reliable, 1: true period could not be unambiguously determined, 0: no periodicity evident. References: A18 (Angus et al. 2018), M13 (McQuillan et al. 2013), M15 (Mazeh et al. 2015), W13 (Walkowicz & Basri 2013). Only a portion of this table is shown here to demonstrate its form and content. A machine-readable version of the full table is available.

2. Compile published rotation period measurements from four sources in the literature (McQuillan et al. 2013; Walkowicz & Basri 2013; Mazeh et al. 2015; Angus et al. 2018).
3. Perform a Lomb-Scargle (L-S) periodogram analysis of the *Kepler* PDPSAP light curve using the `LombScargle` class in the `astropy.timeseries` package.
4. Phase-fold the PDPSAP light curve on the L-S peak power period and any published period, as well as on the first harmonic and sub-harmonic of each of the previously mentioned periods.
5. Generate a vetting sheet including all phase-folded light curves, the L-S periodogram, a 120-day segment of the light curve, and the full light curve.
6. Visually examine each vetting sheet, recording the preferred period source and assigning a reliability flag to each period determination (3 : highly reliable, 2 : reliable, and 1 : period could not be unambiguously determined, and 0 : no periodicity evident).⁴

The results of our rotation period vetting are summarized in Table 1.

3. ANALYSIS

3.1. Evolution of the period-radius diagram: isochrone ages

We first plotted the period-radius (P-R) diagram for CKS planets in four bins of $\log(\text{age})$: < 9.25 , $9.25\text{--}9.5$, $9.5\text{--}9.75$, and ≥ 9.75 for both the filtered and base samples (Figures 2 and 3, respectively).⁵ This binning scheme was in part chosen because there are few planets with $\log(\text{age}) < 9$ or > 10 . From these figures we observed a conspicuous void of planets around the radius valley in the youngest age bin ($\lesssim 1.8$ Gyr). Moreover, the slope of the void appears to be very close to the slope of

⁴ Vetting sheets will be made publicly available after submission.

⁵ The completeness curve in Figures 2 and 3 was computed for CKS stars using CKS stellar parameters and the methodology of Burke et al. (2015) as implemented in Python at <https://dfm.io/posts/exopop/>.

the radius valley determined in [Van Eylen et al. \(2018\)](#), hereafter V18, from a subset of planets orbiting stars with precise asteroseismic parameters. However, while the slope of the young planet void appears to be consistent with that of the radius valley, the intercept appears to be different. This is evident from the fact that the lower boundary of young sub-Neptunes straddles the V18 line, while the super-Earths are well-separated from the V18 valley. In other words, there appears to be a dearth of large super-Earths at younger ages, resulting in an apparent shift in the peak of the super-Earth radius distribution to larger radii at older ages. Our interpretation of this shift is discussed in §4. It is also interesting to note that the majority of the stars hosting planets nominally in the radius valley ($1.6\text{--}1.9 R_{\oplus}$) in the two youngest age bins in Figure 2 appear preferentially more evolved in the H-R diagram relative to stars in the same age bin that do not host planets in the valley.

While age, mass, and metallicity are correlated in the CKS sample, we show that the distribution of masses in each age bin is not changing drastically. The age-metallicity gradient is stronger, and essentially all stars in the youngest age bin are metal-rich. However, it is also clear that stars hosting planets in the radius valley are not exclusively metal-poor but rather have a wide range of metallicities. Additionally, while the [Fe/H] distributions in the two youngest age bins are broadly similar, the distributions of planets in the P-R diagram are markedly different. While these observations offer some degree of assurance that observed features in the P-R diagram are due to age, rather than mass or metallicity, we explore the effects of stellar mass and metallicity further in §3.5 and §3.6.

3.2. Evolution of the period-radius diagram: gyrochronology

To this point we have only considered isochrone ages from F18 in our analysis. While we present a qualitative validation of the F18 ages in Appendix A, there are substantial uncertainties associated with isochrone ages. It is also possible to empirically age-rank the CKS sample with a gyrochronology analysis. Recently, [Curtis et al. \(2020\)](#) presented empirical gyrochrones for several open clusters which enable high-fidelity, model-independent age ranking of solar-type stars with well-determined T_{eff} and rotation periods.

We separated the CKS sample into “fast” rotators and “slow” rotators using the hybrid NGC 6819 + Ruprecht 147 gyrochrone of [Curtis et al. \(2020\)](#), corresponding to an age of ~ 2.7 Gyr. To perform this cut we first converted the gyrochrone from a $(B_P - R_P) - P_{\text{rot}}$ relation into a $T_{\text{eff}} - P_{\text{rot}}$ relation using the color-temperature polynomial relation presented by those authors (valid for the temperatures considered here).⁶

We constructed the young planet sample from the CKS base sample (§2) by choosing host stars placed between the 0.12 Gyr (Pleiades) and 2.7 Gyr gyrochrones in the $T_{\text{eff}} - P_{\text{rot}}$ diagram, high reliability P_{rot} flags, $\text{RUWE} < 1.4$ (to remove unresolved

⁶ We opted not to perform the gyrochronology classification in color space because we noted increased scatter in the $(B_P - R_P) - P_{\text{rot}}$ diagram for CKS stars, possibly a result of reddening, metallicity effects, or both.

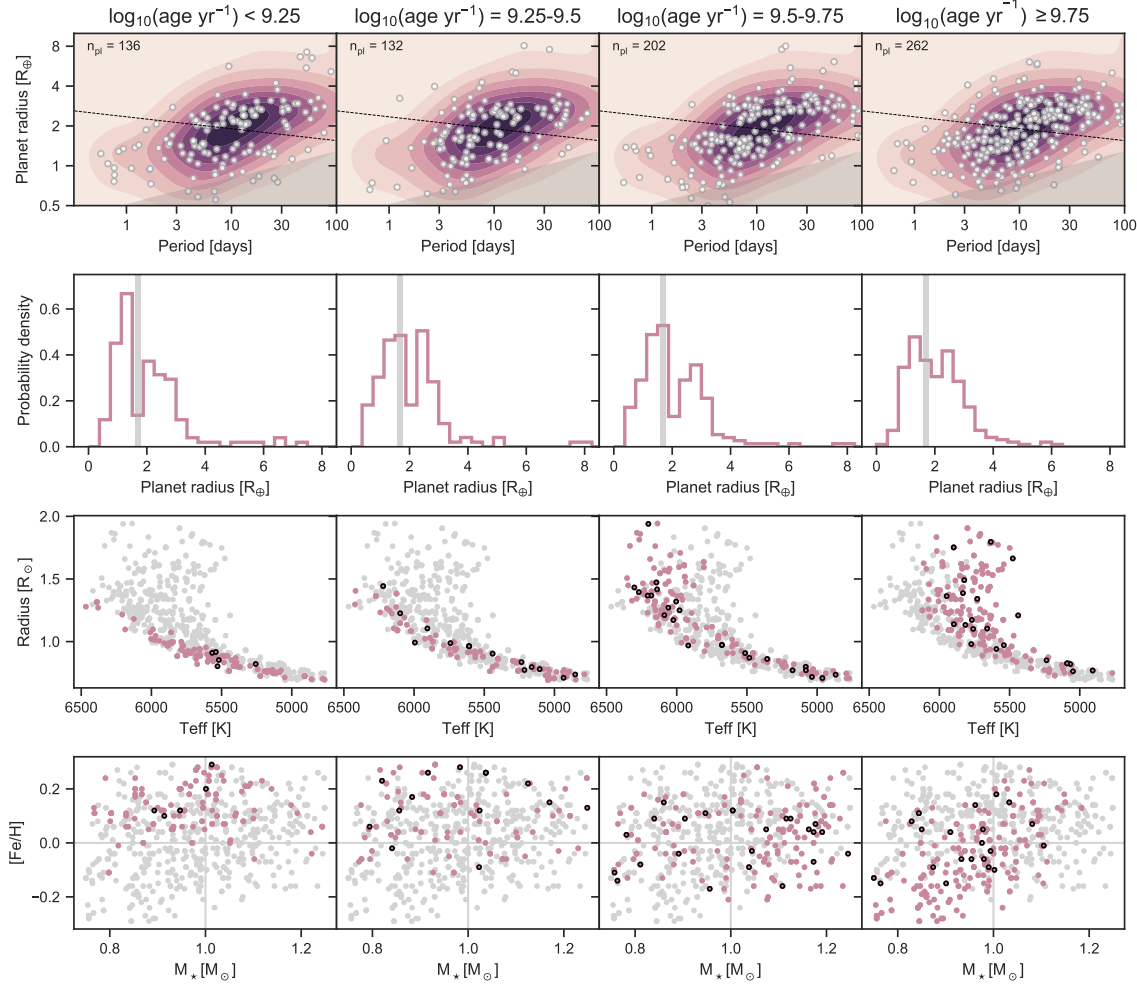


Figure 2. *First row:* Evolution of the *Kepler* planet population in the period-radius diagram for the filtered CKS sample (age bins indicated above each panel). Contours show Gaussian kernel density estimates of planets in the overall CKS sample. The black dashed line indicates the radius valley derived by V18. The grey shaded region indicates the 25% pipeline completeness contour calculated from the CKS sample. *Second row:* one-dimensional distributions of planet radii for the samples plotted above in each case. The nominal location of the radius gap from Fulton et al. (2017) is indicated by the vertical grey stripe. *Third row:* our base CKS planet-host sample in the $T_{\text{eff}}-R_*$ plane (grey) and the host stars in the age bins indicated at the top (pink). Stars hosting planets in the radius range $1.6-1.9 R_{\oplus}$ are outlined in black. *Fourth row:* as in the third row, the distribution of planet hosts in the mass-metallicity plane.

binaries with unreliable rotation periods), and $T_{\text{eff}} < 6000$ K. The $T_{\text{eff}} < 6000$ K cut is motivated by the fact that gyrochrones cluster closely for hotter stars, and small temperature uncertainties can translate to large uncertainties in age from a gyrochronology analysis.

The old rotation-selected planet sample was selected in the same fashion from stars lying *above* the 2.7 Gyr gyrochrone, except for the high reliability P_{rot} flag requirement. We found that we assigned the high reliability flag more often to faster rotators which tend to exhibit higher amplitude and more stable brightness modulations

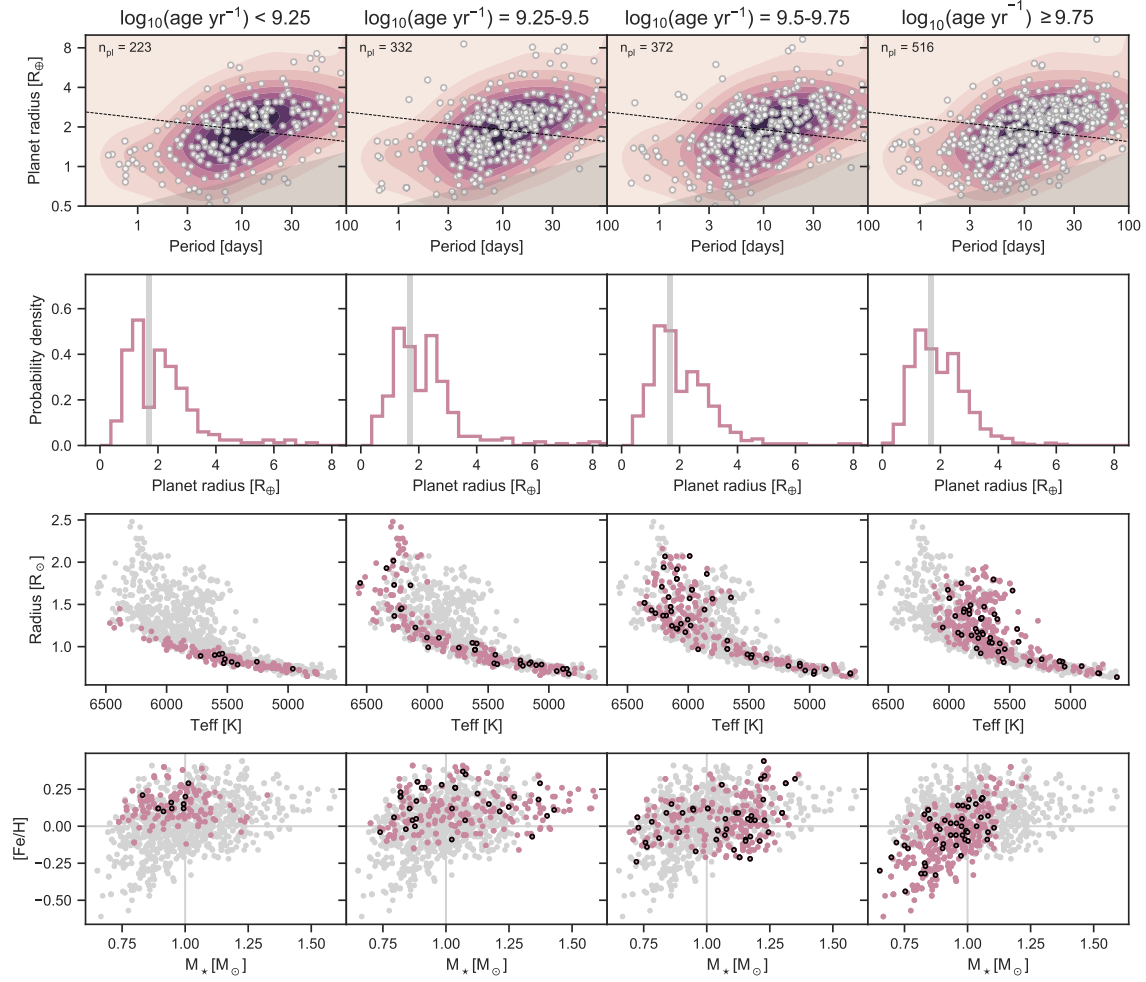


Figure 3. Same as Figure 2 for the base sample.

(presumably due to larger, longer-lived spots), while the older, more slowly rotating stars exhibit smaller-amplitude, more sporadic, Sun-like variations potentially due to smaller, short-lived spots. Thus, in the slow-rotator sample we accepted stars with either reliable or highly reliable P_{rot} flags.

The distributions of the young and old rotation-selected planet hosts in the T_{eff} - P_{rot} and H-R diagrams are shown in Figure 4, along with the 1-d distributions of their median isochrone ages. We observe that the fast rotating sample does indeed correspond to stars that lie closer to the ZAMS with median isochrone ages strongly skewed towards younger ages (mostly below 3 Gyr) relative to the CKS sample. The more slowly rotating stars show a distribution of median isochrone ages which is practically indistinguishable from the bulk of the CKS sample, but with a significant number of stars in the ~ 1 – 3 Gyr range. However, this is likely to be the result of isochrone clustering on the main sequence and not because those stars are actually young. We also note that only 46% (546/1189) of the stars in our sample have assigned rotation periods from our period vetting procedure. For the remaining stars

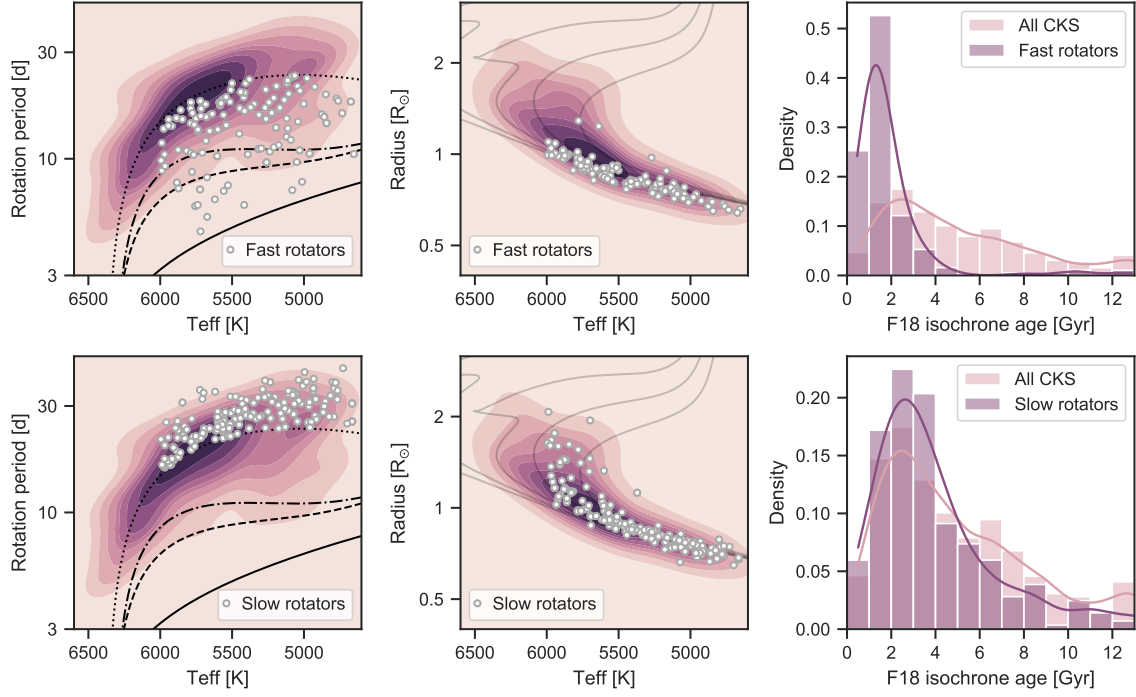


Figure 4. The $T_{\text{eff}}-P_{\text{rot}}$ diagram (left column), H-R diagram (middle column), and median isochrone age distributions (right column) for the young (top row) and old (bottom row) rotation-selected samples. The shaded contours in the left and middle columns show Gaussian kernel density estimates of the full CKS sample in those respective planes. In the left column, the solid, dashed, dash-dotted, and dotted lines indicate polynomial fits to the empirical gyrochrones of the Pleiades ($\log(\text{age}) \approx 8.1$), Praesepe ($\log(\text{age}) \approx 8.8$), NGC 6811 ($\log(\text{age}) \approx 9$), and NGC 6819 + Ruprecht 147 ($\log(\text{age}) \approx 9.4$) clusters respectively (Curtis et al. 2020). In the middle panels, the grey curves show solar-metallicity, non-rotating MIST v1.1 isochrones from $\log(\text{age}) = 9-10$ in steps of 0.25 dex.

it was not possible to unambiguously assign a period. Those stars are preferentially more evolved relative to the periodic sample, though they are observed across the H-R diagram. Thus, the modest decrement at old ages in the age distribution of the slow rotators relative to the overall CKS sample may be the result of a finite active lifetime for solar-type stars.

After separating the planet hosts into the fast and slow rotator samples, we then examined the distributions of the corresponding planet populations in the P-R diagram (Figure 5). We observe qualitatively similar behavior as to what was found when using isochrone ages to perform age cuts. That is, there is a dearth of exoplanets in the radius valley among planets empirically determined to be younger than ~ 2.7 Gyr from a gyrochronology analysis. Among the planets older than ~ 2.7 Gyr the radius valley appears more filled in. Moreover, the slope and boundaries of the radius valley in the left panel of Fig. 5 appear to be very close to that derived from the isochrone age-selected sample (as described in §3.3).

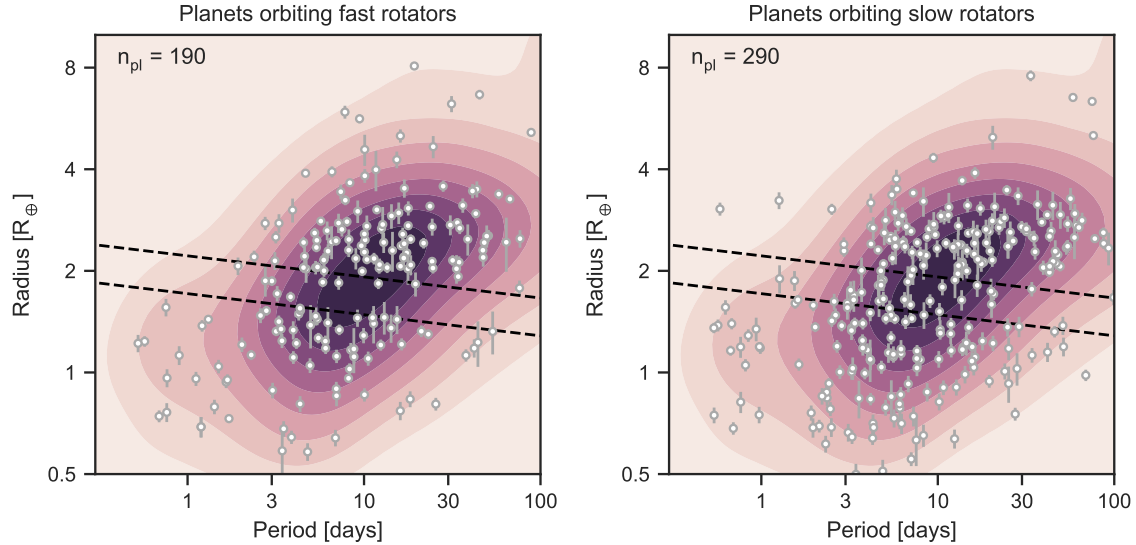


Figure 5. The period-radius diagram for exoplanets orbiting stars rotating more rapidly (left) or more slowly (right) than an empirical 2.7 Gyr gyrochrone. The shaded contours represent a 2D Gaussian kernel density estimation for the overall CKS sample. The black dashed lines indicate the margins of the young planet void *derived from the isochrone-selected sample* in §3.3.

3.3. Measuring the slope of the void

As the slope of the radius valley contains information about the mechanism(s) responsible for producing it, we proceeded to characterize the void for three planetary samples described as follows. Each sample is a subset of the base sample, sharing the following cuts: planets orbiting dwarf stars (described in §2) with $P < 100$ d, $R_P < 10 R_\oplus$, and $\sigma_{R_P}/R_P < 20\%$. Sample A also employs the age restriction $9 < \log(\text{age}) \leq 9.25$, while sample B is produced from the more inclusive criterion $\log(\text{age}) \leq 9.25$. Finally, sample C combines the common cuts with the following criteria: $T_{\text{eff}} < 6000$ K, RUWE < 1.4 , high reliability rotation periods (reliability flag of 3), and positions in the $T_{\text{eff}}-P_{\text{rot}}$ plane between the empirical Pleiades and NGC 6819+Ruprecht 147 gyrochrones of [Curtis et al. \(2020\)](#). The distributions of these planetary samples in the P-R and insolation-radius planes are depicted in Figure 6.

Following the approach of V18 we used support vector machines (SVMs) to find the decision boundary that maximizes the margins between two distinct classes of planets in the period-radius and insolation-radius planes. To label the planets we found that shifting the V18 radius valley equation downwards by 0.07 in $\log_{10}(R_P/R_\oplus)$ provided an unambiguous separation of planets into two classes for sample A. Thus, we used the equation, $\log_{10}(R_P/R_\oplus) = -0.09 \log_{10}(P/\text{d}) + 0.3$, to label planets as sub-Neptunes or super-Earths. To implement the SVM classification we used the `sklearn.svm.SVC` module in Python with a linear kernel ([Pedregosa et al. 2011](#)).

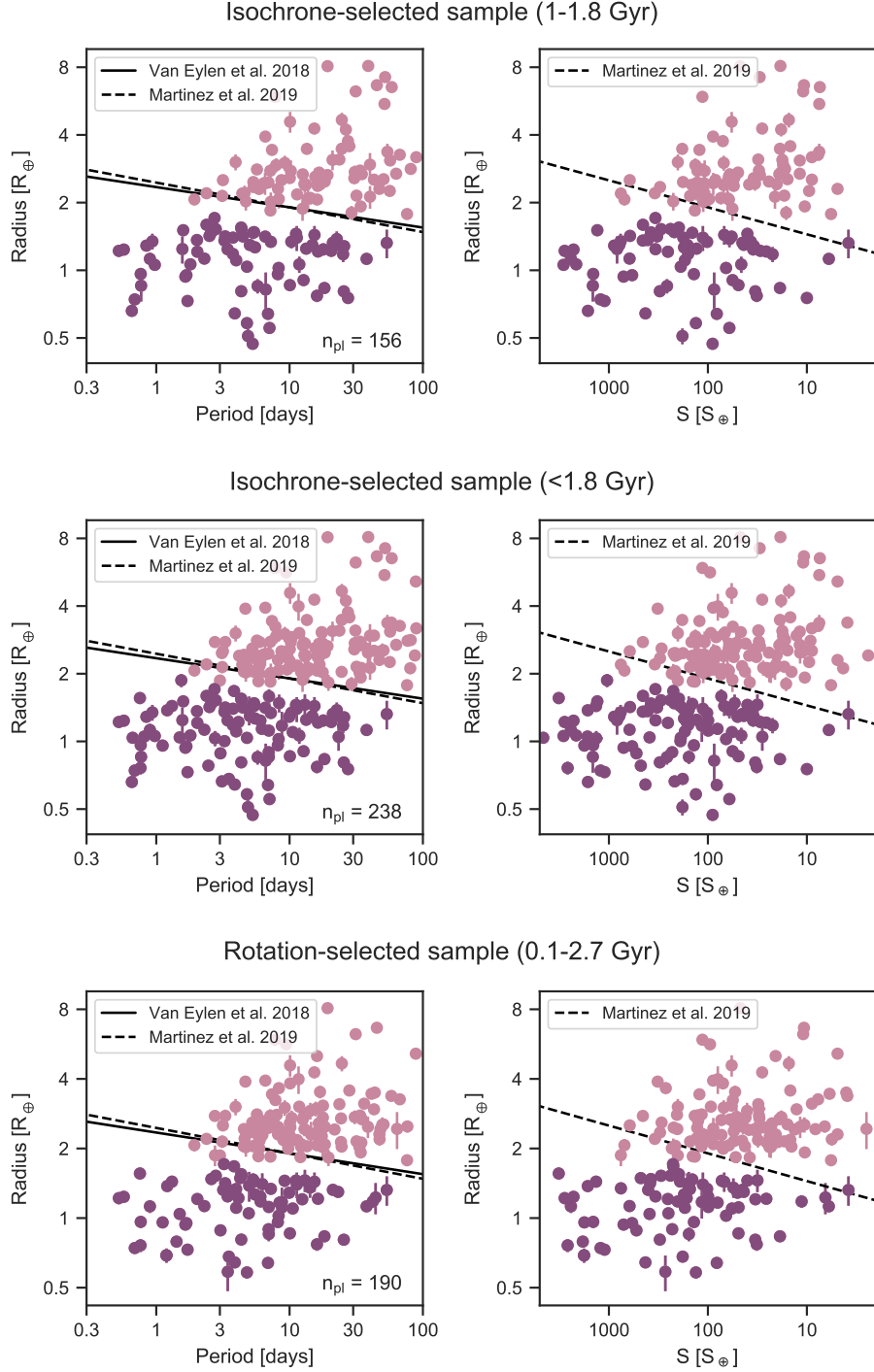


Figure 6. Age-selected samples of *Kepler* planets in the period-radius (left column) and insolation-radius (right column) planes. Age selections are described in §2. Previously determined equations for the radius valley are shown as the black lines. Point colors indicate the classification used in the SVM analysis (described in §3.3).

We explored the sensitivity of our results to the regularization parameter, \mathcal{C} , finding that for $\mathcal{C} < 5$ the SVM misclassifies a large fraction of planets and fails to trace the center of the void which is so readily visible by eye (Figure 7). In determining the equation of the void we ultimately adopt the slope and intercept derived from the $\mathcal{C} = 10$ case, but recommend $\mathcal{C} = 1000$ for determining the upper and lower boundaries of the void. To calculate uncertainties on the slope and intercept of the radius valley, we performed 10^3 bootstrapping simulations, selecting 50 planets (with replacement) randomly from the young planet samples and recording the slope and intercept resulting from the SVM classification for each bootstrapped sample.

Table 2 lists the slopes and intercepts for the young planet void inferred from the SVM bootstrapping simulations. Figures 8 and 9 show the derived radius valley from the bootstrapping simulations and Figure 10 shows the distributions of slopes and intercepts from this analysis. For the \mathcal{C} values explored here, the inferred slopes and intercepts of the radius valley are relatively constant. We find in almost all cases that the slope of the valley is consistent with the slope found in V18 at the $\lesssim 1\sigma$ level. However, we find an intercept that is systematically smaller than that found by V18 and [Martinez et al. \(2019\)](#), by at least 2σ and in some cases as much as 10σ using the quoted uncertainties from those works. While the statistical significance of this difference is highly dependent on the adopted uncertainty (where ours appear to generally be larger), it is clear from Figure 6 that the void we observe is offset from previous determinations of the radius valley. We note that previous works characterized the radius valley among samples with a broader range of ages, while the focus of this analysis is on the younger planets in the CKS sample. In §4 we discuss our interpretation of this difference. The level of agreement between the radius valley slopes derived here and in V18 is noteworthy given that the samples we characterize are $\approx 30\text{--}100\%$ larger and selected on the basis of age, rather than radius precision which was the impetus for the V18 sample.

The upper and lower boundaries of the radius valley are given by the equation:

$$\log_{10}(R_P/R_{\oplus})_{\text{lower}}^{\text{upper}} = \alpha \log_{10}(P/d) + \beta \pm \gamma \sqrt{1 + \alpha^2}, \quad (2)$$

in the period-radius plane or,

$$\log_{10}(R_P/R_{\oplus})_{\text{lower}}^{\text{upper}} = \delta \log_{10}(S_{\text{inc}}/S_{\oplus}) + \epsilon \pm \zeta \sqrt{1 + \alpha^2}, \quad (3)$$

in the insolation-radius plane. We use the highest \mathcal{C} parameter explored here for determination of the radius valley boundaries as it provides the closest match to the data (i.e. the fewest planets inside those boundaries).

3.4. Calculation of false alarm probability

To determine whether the void we observe in the period-radius diagram could be due to chance, we performed simulations to determine the probability of finding n_{itv} or fewer planets in the void from N planets selected at random (without replacement)

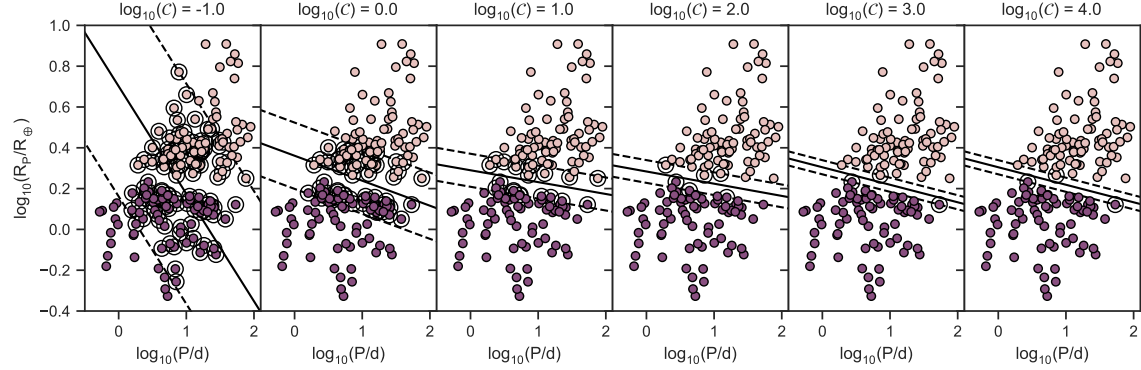


Figure 7. The effect of the regularization parameter, \mathcal{C} , on the support vector classification for young CKS planets (sample A) in the period-radius diagram. In each panel point colors indicate the planet classification provided in the SVM classification analysis. Points encircled by black rings indicate the support vectors. The solid lines indicate the decision surface of maximal separation, while the dashed lines indicate the margins (as discussed in the text).

Table 2. Results of SVM bootstrapping simulations.

Sample	\mathcal{C}	α	β	γ	δ	ϵ	ζ
A	5	$-0.09^{+0.06}_{-0.06}$	$0.33^{+0.06}_{-0.07}$	$0.14^{+0.01}_{-0.01}$	$0.06^{+0.04}_{-0.05}$	$0.13^{+0.12}_{-0.06}$	$0.14^{+0.01}_{-0.01}$
A	10	$-0.08^{+0.06}_{-0.04}$	$0.31^{+0.05}_{-0.05}$	$0.11^{+0.01}_{-0.01}$	$0.06^{+0.03}_{-0.04}$	$0.13^{+0.11}_{-0.04}$	$0.11^{+0.01}_{-0.01}$
A	100	$-0.06^{+0.02}_{-0.04}$	$0.29^{+0.02}_{-0.04}$	$0.07^{+0.01}_{-0.01}$	$0.04^{+0.02}_{-0.03}$	$0.15^{+0.04}_{-0.06}$	$0.07^{+0.01}_{-0.01}$
A	1000	$-0.06^{+0.02}_{-0.04}$	$0.29^{+0.03}_{-0.03}$	$0.06^{+0.01}_{-0.01}$	$0.04^{+0.04}_{-0.01}$	$0.15^{+0.04}_{-0.08}$	$0.05^{+0.01}_{-0.01}$
B	5	$-0.1^{+0.07}_{-0.05}$	$0.32^{+0.06}_{-0.06}$	$0.14^{+0.01}_{-0.01}$	$0.08^{+0.04}_{-0.05}$	$0.07^{+0.1}_{-0.09}$	$0.14^{+0.01}_{-0.01}$
B	10	$-0.08^{+0.05}_{-0.05}$	$0.3^{+0.04}_{-0.07}$	$0.11^{+0.01}_{-0.01}$	$0.06^{+0.04}_{-0.04}$	$0.11^{+0.08}_{-0.07}$	$0.11^{+0.01}_{-0.01}$
B	100	$-0.07^{+0.04}_{-0.04}$	$0.29^{+0.04}_{-0.05}$	$0.06^{+0.01}_{-0.01}$	$0.04^{+0.04}_{-0.03}$	$0.15^{+0.06}_{-0.06}$	$0.06^{+0.01}_{-0.01}$
B	1000	$-0.08^{+0.07}_{-0.03}$	$0.3^{+0.04}_{-0.05}$	$0.05^{+0.01}_{-0.02}$	$0.05^{+0.02}_{-0.04}$	$0.13^{+0.08}_{-0.07}$	$0.05^{+0.01}_{-0.02}$
C	5	$-0.09^{+0.08}_{-0.04}$	$0.3^{+0.04}_{-0.08}$	$0.14^{+0.01}_{-0.01}$	$0.06^{+0.04}_{-0.04}$	$0.11^{+0.09}_{-0.07}$	$0.14^{+0.01}_{-0.01}$
C	10	$-0.06^{+0.06}_{-0.04}$	$0.28^{+0.05}_{-0.05}$	$0.11^{+0.01}_{-0.01}$	$0.05^{+0.03}_{-0.03}$	$0.14^{+0.06}_{-0.05}$	$0.11^{+0.01}_{-0.01}$
C	100	$-0.05^{+0.04}_{-0.03}$	$0.27^{+0.03}_{-0.05}$	$0.06^{+0.01}_{-0.01}$	$0.03^{+0.02}_{-0.04}$	$0.17^{+0.06}_{-0.05}$	$0.06^{+0.01}_{-0.01}$
C	1000	$-0.03^{+0.02}_{-0.06}$	$0.26^{+0.04}_{-0.04}$	$0.05^{+0.02}_{-0.01}$	$0.02^{+0.05}_{-0.02}$	$0.17^{+0.07}_{-0.07}$	$0.05^{+0.01}_{-0.02}$

NOTE—Equation for the radius valley in the period-radius diagram is of the form $\log_{10}(R_P/R_\oplus) = \alpha \log_{10}(P/d) + \beta$. In the insolation-radius diagram it is $\log_{10}(R_P/R_\oplus) = \delta \log_{10}(S_{\text{inc}}/S_\oplus) + \epsilon$. Adopted values in bold.

from the CKS sample. Here N is the total number of planets in each of the samples described in §2, i.e. 156, 238, and 190 for samples A, B, and C, respectively. The definition of the radius valley boundaries and hence the true number of planets in the valley, $n_{\text{itv, true}}$, are sensitive to the regularization parameter, \mathcal{C} , and the specific sample used in the SVM bootstrapping analysis (see Figure 11). For each sample and each \mathcal{C} value we performed 10^4 simulations, selecting N planets randomly (without replacement) from the overall CKS sample, modeling the planet period and radius

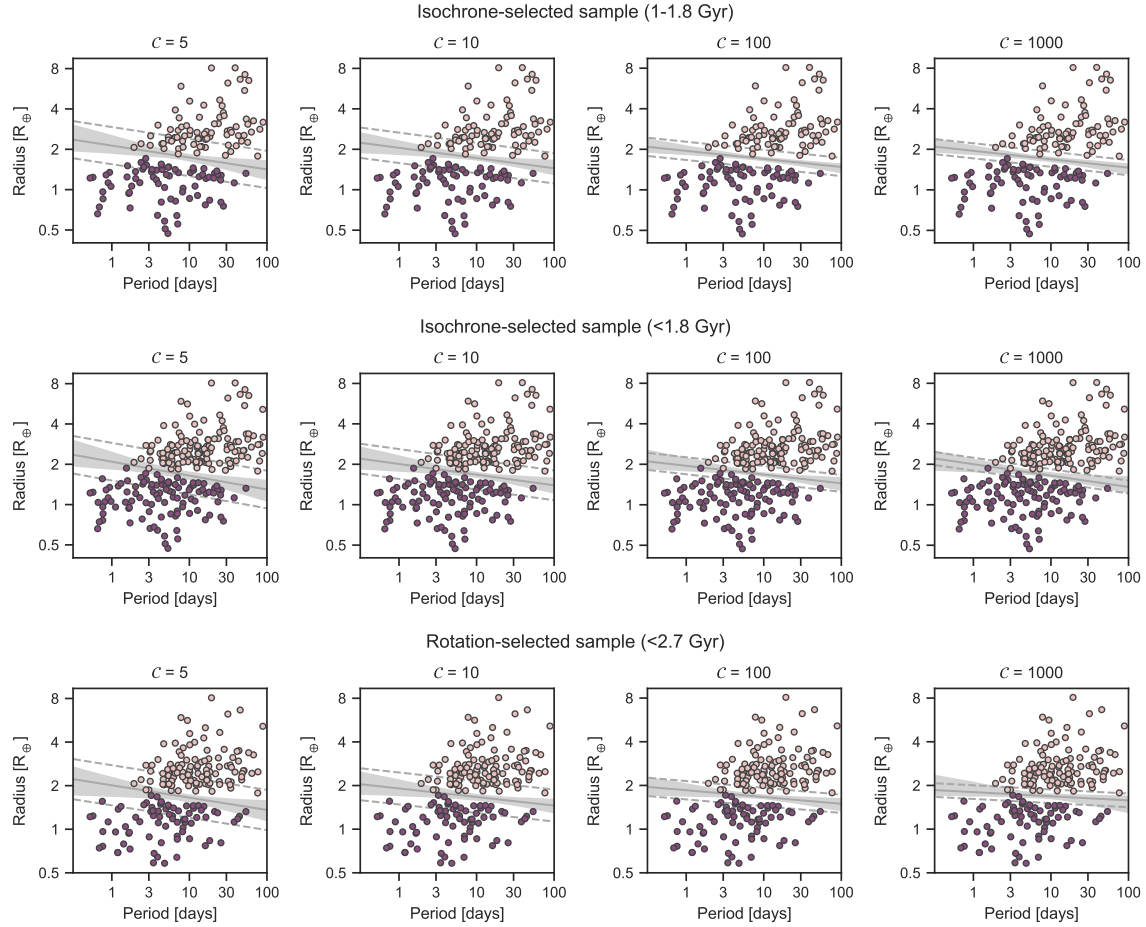


Figure 8. Period-radius diagram for *Kepler* planets in samples A (top row), B (middle row) and C (bottom row). Point colors indicate the classifications used in the support vector machine (SVM) analysis. The grey line and shaded region show the median and 16th-84th percentile width of the radius valley from the SVM bootstrapping simulations. The dashed lines indicate the median margins from the SVM analysis. The regularization parameter, \mathcal{C} , is indicated at the top of each panel.

uncertainties with normal distributions, and recording the number of planets in the valley, $n_{\text{itv,sim}}$. The false alarm probability was then computed as the fraction of total trials which satisfied the condition $n_{\text{itv,sim}} \leq n_{\text{itv,true}}$. The results of these simulations are tabulated in Table 3. For $\mathcal{C} = 5$, we find false alarm probabilities in the range of 18–30%, but from Figure 11 it is clear that the SVM margins in this case are so wide as to not provide an accurate description of the void boundaries. The same may be argued for the $\mathcal{C} = 10$ case, but even then we find false alarm probabilities <10%. Finally, for the $\mathcal{C} = 100, 1000$ cases, for which the SVM margins precisely trace the boundaries of the void, we found false alarm probabilities $\ll 1\%$.

We also performed Monte Carlo simulations to estimate the probability that the void could be produced from random selection among those planets orbiting hosts rotating more slowly than the empirical 2.7 Gyr gyrochrone (see Fig. 4). We started by performing the same generic cuts on the overall CKS sample as were performed on

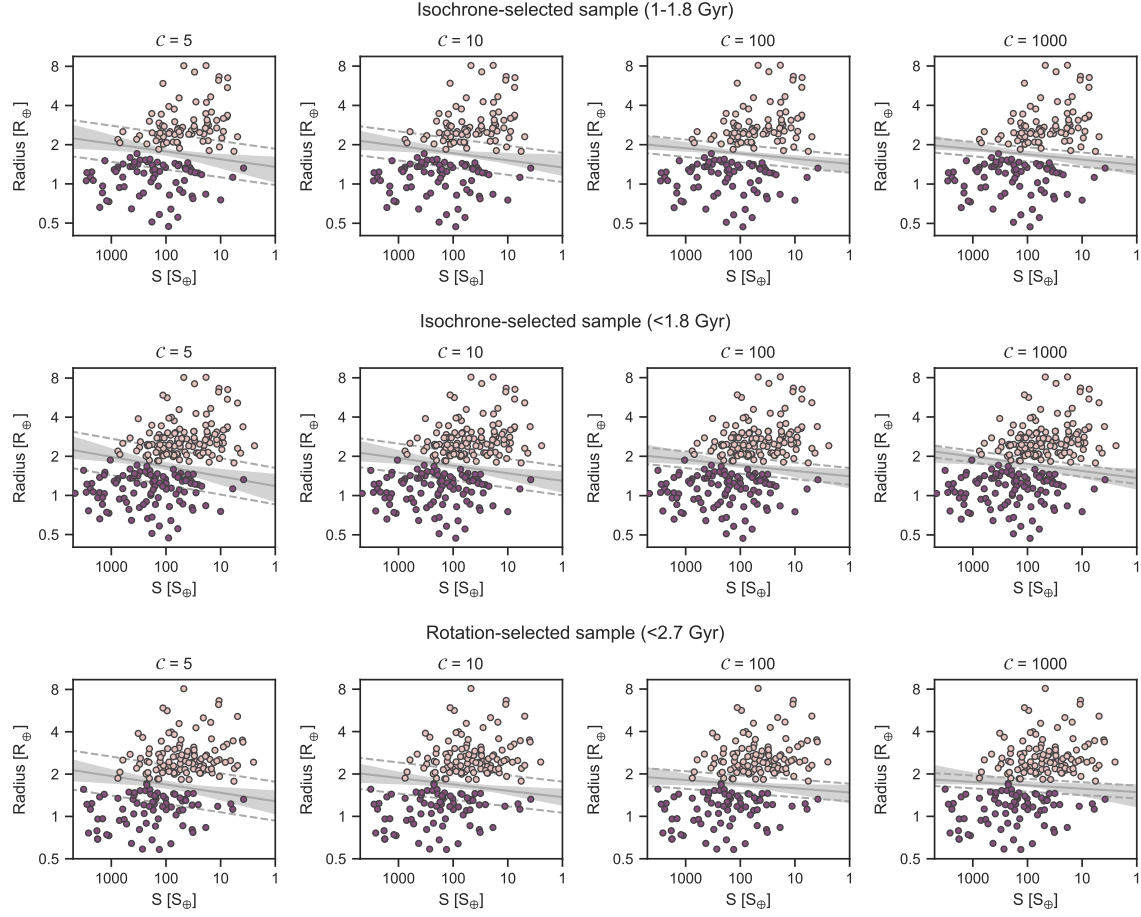


Figure 9. Same as Figure 8 for the insolation-radius plane.

the rotation-selected sample (main-sequence stars, no false positives, $\text{RUWE} < 1.4$, $T_{\text{eff}} < 6000$ K, and planets with $P < 100$ d, $R_P < 10 R_{\oplus}$, and radius precision $< 20\%$). Then, in 10^4 simulations we modeled the uncertainties in the planet periods and radii using normal distributions, selected 190 planets at random (without replacement) from the slow rotator sample, and computed the number of planets in the void. Here, 190 is the total number of planets in the fast rotator sample. We found that the probability of finding a comparably empty void from the slow rotator sample is $< 2\%$ when using the sample C margins and $C = 100, 1000$. Using the same C values but margins derived from the isochrone samples raises the false alarm probability, but only to $\sim 2\text{--}6\%$ at most. Taken together, we conclude that the emptiness of the observed void is not due to chance.

3.5. Effects of stellar mass and metallicity

Our analysis separates the data set into age bins in order to understand the evolution of planets on a population level. Since age, mass, and metallicity are correlated in the CKS sample, it is difficult to entirely disentangle the effects of each parameter on the distribution of planets in the P-R diagram. We explored how sensitive our analysis

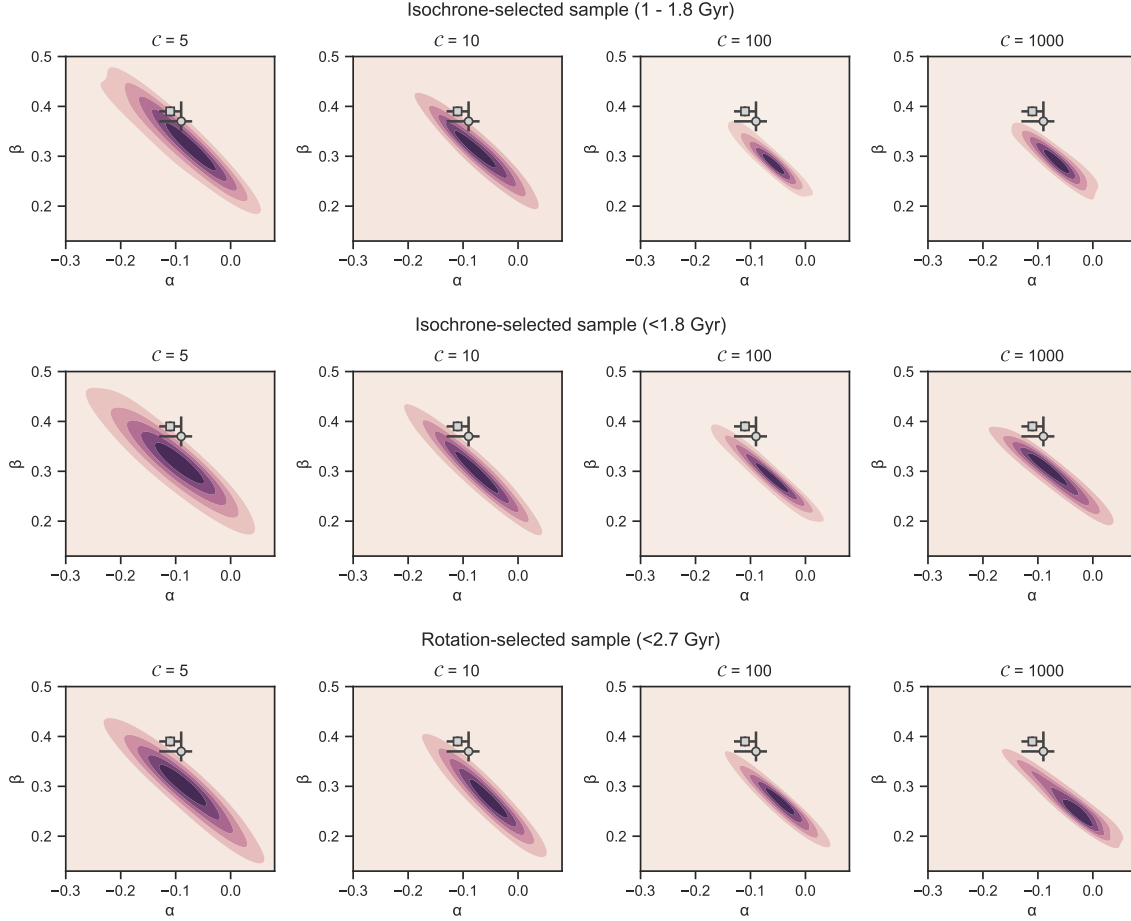


Figure 10. Gaussian kernel density estimation of the distribution of radius valley slopes (α) and intercepts (β) from the SVM bootstrapping simulations with different regularization (\mathcal{C}) parameters. The circle with errorbars indicates the values derived in [Van Eylen et al. \(2018\)](#) from planets orbiting asteroseismic stars. The square with errorbars indicates the values derived by [Martinez et al. \(2019\)](#) from an independent spectroscopic analysis of the CKS sample.

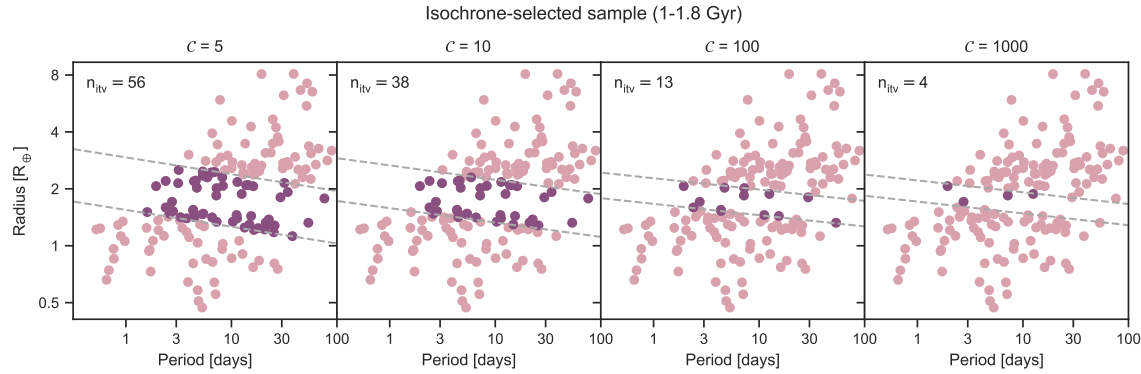


Figure 11. The effect of regularization parameter, \mathcal{C} , on the boundaries of the radius valley (indicated by the dashed lines) and hence the number of planets in the valley (dark points). Sample A is shown for illustration.

Table 3. False alarm probabilities.

Sample	$\mathcal{C}=5$	$\mathcal{C}=10$	$\mathcal{C}=100$	$\mathcal{C}=1000$
A	30%	3.0%	0.09%	< 0.01%
B	18%	6.5%	0.08%	0.01%
C	22%	4.5%	0.03%	0.08%

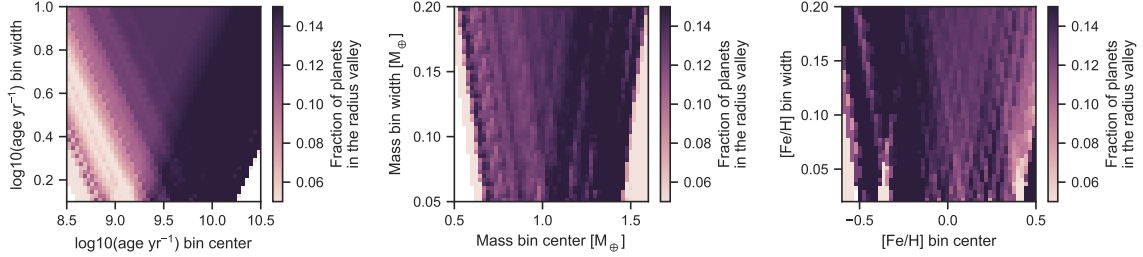


Figure 12. Effects of binning schemes (in age, mass, and metallicity from left to right) on the fractional occupancy of the radius valley. Note the color scaling is the same for each panel.

is to specific binning schemes by recording the fractional number of planets in the valley over a two-dimensional grid of bin centers and bin widths in age, mass, and metallicity. We used the definition of the radius valley boundaries expressed in §3.3 for this purpose (specifically, the margins given by the $\mathcal{C} = 1000$, sample A case).

Figure 12 shows the results of this exercise; the young planet void is apparent as the light, broad diagonal stripe in the left panel. For small bin widths, the minimum density of the radius valley is achieved for a bin center between $9 < \log(\text{age}) < 9.25$. This is unsurprising, as the boundaries of the radius valley were identified in and derived for just such a binning strategy. However, as the bin width in $\log(\text{age})$ increases, the minimum density of the valley shifts systematically towards younger bin centers. This suggests that the filling of the radius valley is due to preferentially older planets. Fig. 12 also reveals that there is no binning strategy in mass or metallicity that can produce a comparably empty void (in a fractional sense) except in finely tuned regions of parameter space where sample sizes are small. However, while not as pronounced, we do note the radius valley (as defined in this exercise) appears emptier for lower-mass stars and metal-rich stars. The latter observation is consistent with the finding of an apparently wider radius valley for metal-rich hosts within the CKS sample (Owen & Murray-Clay 2018), though we note that age and $[\text{Fe}/\text{H}]$ are anti-correlated.

We also examined the one-dimensional radius and period distributions for CKS planets in the extremes of the stellar age, mass, and metallicity axes (Figure 14). The purpose of this exercise was to highlight any exoplanet demographic trends as a function of these key stellar parameters. Interestingly, even without completeness

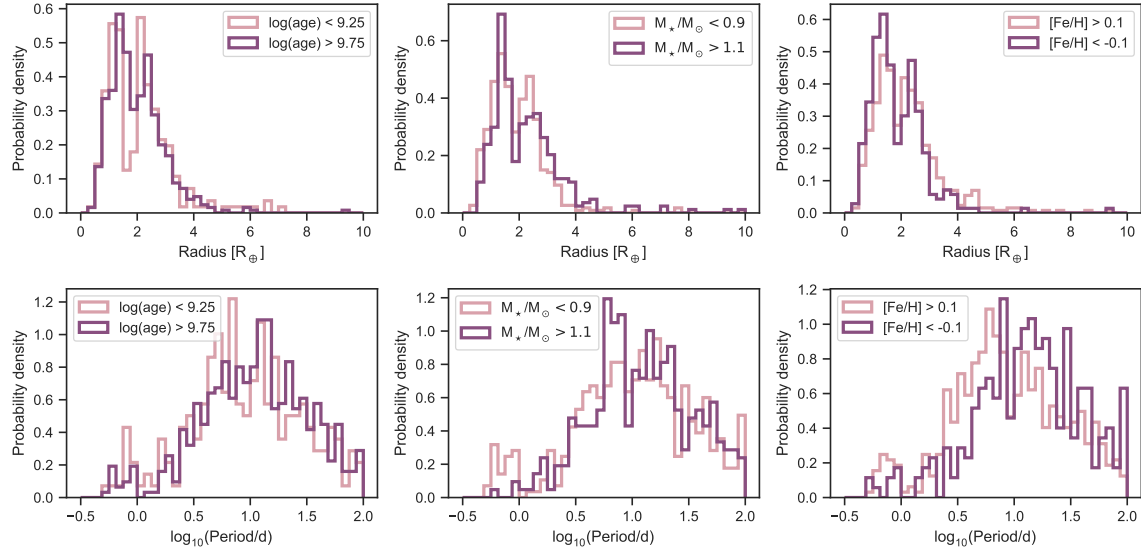


Figure 13. Planet radius (top row) and period (bottom row) distributions among our CKS base sample for host stars of different age (left column), mass (middle column), and metallicity (right column).

corrections or occurrence rate calculations, several of the now well-established trends in the *Kepler* planet population are evident from Figure 13: larger sub-Neptunes around more massive stars (Fulton & Petigura 2018; Wu 2019; Cloutier & Menou 2020) and more metal-rich stars (Petigura et al. 2018), the rising occurrence of ultra-short period ($P < 1$ d) planets with decreasing stellar mass (Sanchis-Ojeda et al. 2014), and the rising occurrence of short-period planets ($1 < P < 10$ d) of all sizes with increasing metallicity (Petigura et al. 2018). The other trend that is apparent is the dearth of planets in the radius valley for young stars. The trend of a wider radius valley around more metal-rich stars found by Owen & Murray-Clay (2018) is not immediately obvious, but relative to that study we use updated planetary radii from F18, do not include completeness corrections, and perform slightly different cuts.

3.6. In what ways are planets in the valley different?

In an effort to quantify the parameters that are most important in contributing to the filling of the radius valley, we performed a two-sided Anderson-Darling (A-D) test with `scipy.stats.anderson_ksamp` to test the null hypothesis that the distribution of a given variable for stars hosting planets in the valley was drawn from the same distribution of that parameter among our base CKS sample.

The results of this exercise are summarized in Table 4 and select parameter distributions are shown in Figure 14. In this exercise we have assumed the equation for the radius valley and its boundaries are given by the fourth row of Table 2. Additionally, for each parameter we restrict our analysis to those CKS stars/planets for which that parameter is defined (i.e. we exclude targets missing data for a given variable). We also apply the common cuts described in §3.3 before performing the A-D tests. In the

case of P_{rot} , we also restricted the sample to $T_{\text{eff}} < 6000 \text{ K}$, where rotation periods are more reliable indicators of age.

Of the nine parameters with the highest normalized k-sample A-D test statistics (and p -values < 0.05), all but two pertain directly or indirectly to the star's evolutionary state: P_{rot} from various sources, P_{rot} flag, R_{var} (a measure of the photometric variability amplitude), the median posterior age from isochrones, and R_{\star} . The other two parameters are fractional R_P precision and r_8 (a measure of flux dilution). Thus, of the parameters investigated, those which contribute most to the filling of the radius valley either relate to stellar age or may be associated with erroneous measurements of the planetary radii. Inspection of the parameter distributions (like those shown in Fig. 14) reveals that planets in the valley tend to orbit stars which are older, larger, less likely to have a securely detected rotation period, rotating more slowly, and photometrically quieter. Planets in the valley also have lower r_8 values relative to the CKS base sample. Naïvely, one might expect higher r_8 values among planets in the radius valley as flux dilution can lead to erroneous planet radius measurements. However, planets in the radius valley are by definition small, so it is perhaps not surprising that there is a preference for stars not affected by crowding.

We also found that the stellar mass and metallicity distributions for stars hosting planets in the radius valley are statistically indistinguishable from those of CKS base sample. This lends further support to the notion that the feature identified in the CKS data set from age selections is not due to correlations between stellar age, mass, and metallicity.

The parameter which appears to be most important in contributing to the filling of the radius valley is planet radius precision. This suggests that the radius valley may be emptier than is suggested by current data. The fractional stellar radius precision does not, however, contribute to the filling of the valley. This is not surprising as the typical error budget for a planet's radius in the CKS sample is dominated by the R_P/R_{\star} uncertainty from light curve fitting rather than the stellar radius uncertainty (Petigura 2020). In §3.7 we examine the possibility that a correlation between planet radius precision and age could conspire to produce the observed void.

3.7. *Confounding scenarios*

A possibility not yet explored is that the radius valley is inherently empty but, for some reason, planets orbiting stars with younger assigned ages in the CKS sample have more precise radii. In §3.6 we established that the planet radius precision is the most important parameter contributing to the filling of the radius valley. We quantified the correlation between fractional planet radius precision and $\log(\text{age})$ by computing the Spearman rank correlation coefficient for planets with $P < 100 \text{ d}$, $R_P < 10 R_{\oplus}$, non-false positive dispositions, and main-sequence host stars (filters 1,2,4, and 5 from §2). We used the `scipy.stats.spearmanr` function for this purpose and found a small p -value (2×10^{-4}) but a very weak correlation coefficient ($\rho < 0.1$).

Table 4. Results of k-sample Anderson-Darling tests.

Parameter	Ref.	A-D test stat.	A-D p-value	Sample size (valley/control)
σ_{R_P}/R_P	F18	14.2986	0.0010	196/1443
P_{rot} flag	D20	6.0809	0.0015	196/1443
P_{rot}	M15	4.8232	0.0040	135/1055
R_{var}	M15	4.6740	0.0045	180/1334
log(age)	F18	4.3677	0.0059	196/1443
R_*	F18	3.6118	0.0113	196/1443
r_8	F18	2.5298	0.0298	196/1443
P_{rot}	M13	2.1713	0.0415	36/371
P_{rot}	D20	1.9495	0.0511	55/592
P_{rot}	A18	0.6685	0.1749	109/873
SNR_1	D20	0.6517	0.1778	190/1420
T_{eff}	F18	0.6183	0.1837	196/1443
R_{τ}	P20	0.2980	0.2500	190/1415
σ_{R_*}/R_*	F18	0.2516	0.2500	196/1443
M_*	F18	0.2118	0.2500	196/1443
Parallax	F18	0.0956	0.2500	196/1443
CDPP3	D20	-0.1594	0.2500	190/1420
P_{rot}	W13	-0.1897	0.2500	34/335
A_V	B20	-0.5039	0.2500	188/1390
G mag	DR2	-0.5572	0.2500	190/1420
A_v	L20	-0.5705	0.2500	187/1382
[Fe/H]	F18	-0.6303	0.2500	196/1443
RUWE	D20	-0.6390	0.2500	190/1418
RCF	F18	-0.9397	0.2500	55/423

NOTE—References: A18 (Angus et al. 2018); D20 (this work); DR2 (Gaia Collaboration et al. 2018); F18 (Fulton & Petigura 2018); L20 (Lu et al. 2020); M15 (Mazeh et al. 2015); M13 (McQuillan et al. 2013); P20 (Petigura 2020); W13 (Walkowicz & Basri 2013)

To further investigate the impact of radius precision we computed the fraction of planets in the valley for young and old samples as a function of fractional radius precision allowed. For a given sample of planets and over a grid of radius precision thresholds, we selected the planets with fractional radius uncertainties smaller the threshold value and computed the ratio of planets in the valley to the total number of planets meeting the radius precision requirement. We performed 10^3 bootstrapping simulations (including modeling of the planet radii as normal distributions) to determine the uncertainties on these trends, which are shown in Figure 15. We found that the radius valley is comparably empty for young and old planets if the fractional radius precision is required to be better than $\sim 5\%$. However, this is not unexpected as our CKS base sample size diminishes steeply below fractional radius uncertainties of 7%. For reference, the median fractional radius uncertainties for the CKS base sample, young isochrone age-selected sample (sample B), and old isochrone age-selected sample are 5.0%, 4.5%, and 5.2%, respectively.

Finally, we examined the one-dimensional radius distributions for the young and old isochrone age-selected samples with planet radii known to better than 5%. We

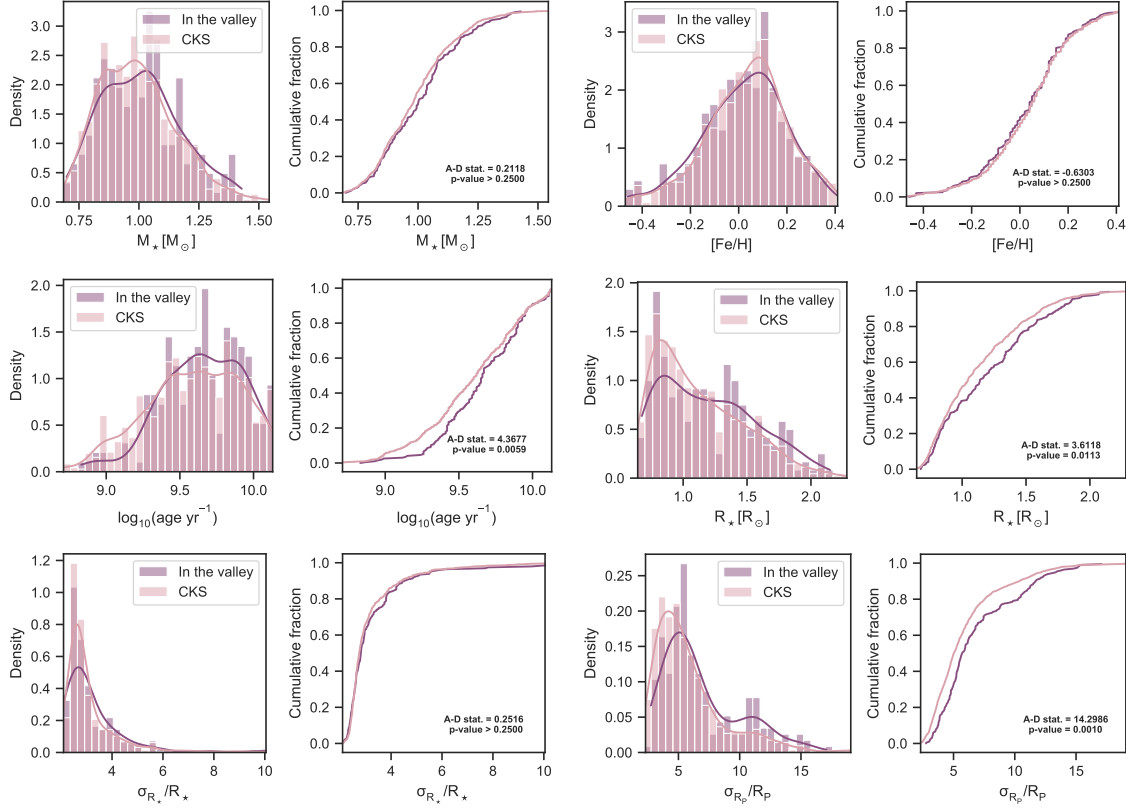


Figure 14. Planet radius (top row) and period (bottom row) distributions for host stars of different age (left column), mass (middle column), and metallicity (right column). Distributions shown are for our CKS base sample.

performed 10^3 bootstrapping simulations (again modeling the planet radii as normal distributions) to determine uncertainties on these distributions. The results are shown in Figure 16. While radius precision is clearly an important parameter in determining the occupancy of the radius valley, we conclude that it is unlikely to explain the entire deficit observed for the young planet sample.

3.8. Accounting for age uncertainties

In §3.4 we assessed the probability that the observed void was due to chance selection of planets from the overall CKS data set, and in §3.5 we explored the sensitivity of the void occupancy to binning schemes in mass, age, and metallicity. Here we attempt to account for stellar age uncertainties in examining the void occupancy as a function of age. As discussed in the Appendix, there may be substantial uncertainties in stellar ages, particularly if those ages originate from isochrones. As a result, when binning in stellar age there is considerable uncertainty in the degree of contamination by stars with inaccurate ages.

To mitigate the effect of stars with spurious ages, we performed Monte Carlo simulations in which the ages were modeled as normal distributions in $\log(\text{age})$ centered on the median values published in F18 with widths taken as the maximum of the lower and upper age uncertainties for each star. While this is not the same as draw-

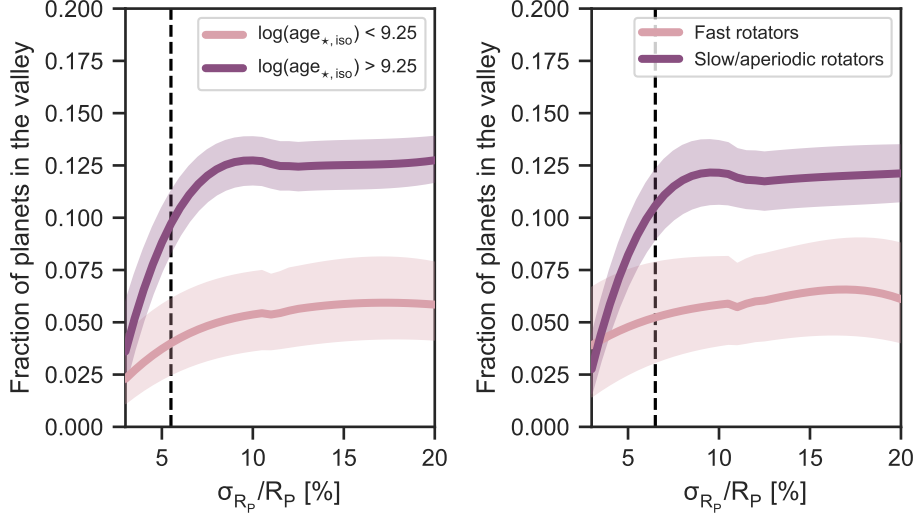


Figure 15. Fraction of planets in the radius valley as a function of maximum fractional radius uncertainty. For each age-selected sample shown, the fraction of planets in the valley is computed for the subsample of planets with fractional radius uncertainties lower than the value on the ordinate. Solid lines and shaded bands show the median and 16th–84th percentile range from bootstrapping simulations, respectively. In each panel the fiducial dashed line shows the value of fractional radius uncertainty for which both young and old samples contain more than 150 planets (corresponding to 21 ± 4 expected planets in the valley if selected at random from the CKS base sample).

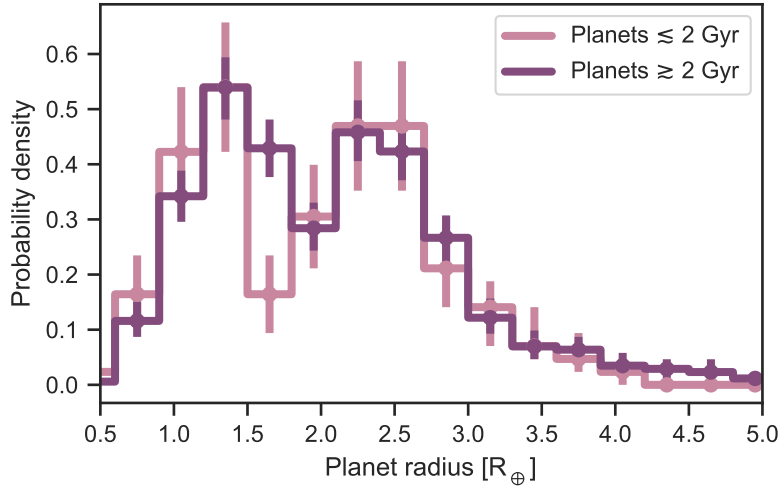


Figure 16. Small planet size distributions among CKS planets with fractional radius uncertainties better than 5%. Uncertainties (the 16th and 84th percentiles) determined from bootstrapping simulations with planet radii modeled as normal distributions.

ing from the empirical posterior probability density functions in age (which are not available) it is a crude proxy. For 50 bin centers in $\log(\text{age})$ from 8.25–10.25 we then performed 10^3 Monte Carlo simulations in each bin, randomly generating ages as described above, to measure the fraction of planets in the valley as a function of age. We measured the fraction of planets in the valley relative to the total number of

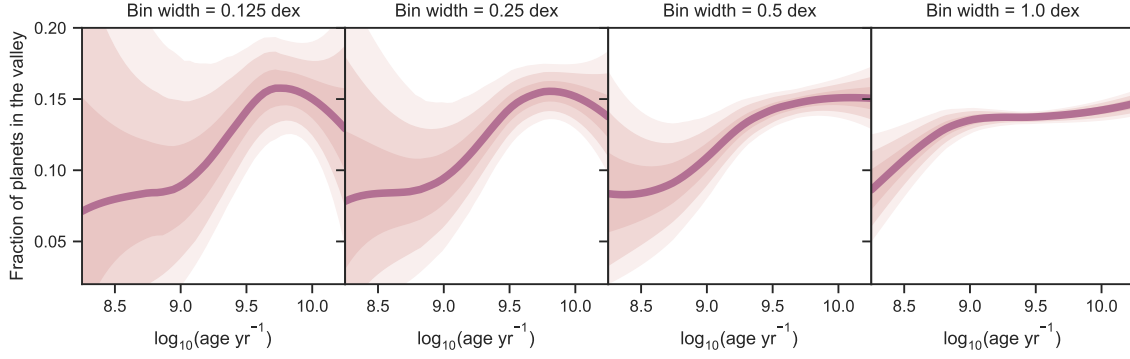


Figure 17. Results of Monte Carlo simulations exploring the occupancy of the radius valley as a function of age, accounting for uncertainties in stellar ages. The dark line shows the median trend resulting from the simulations while the shaded contours show the 68.3, 95.4, and 99.7 percentile ranges. The curves have been smoothed with a Savitzky-Golay filter for clarity.

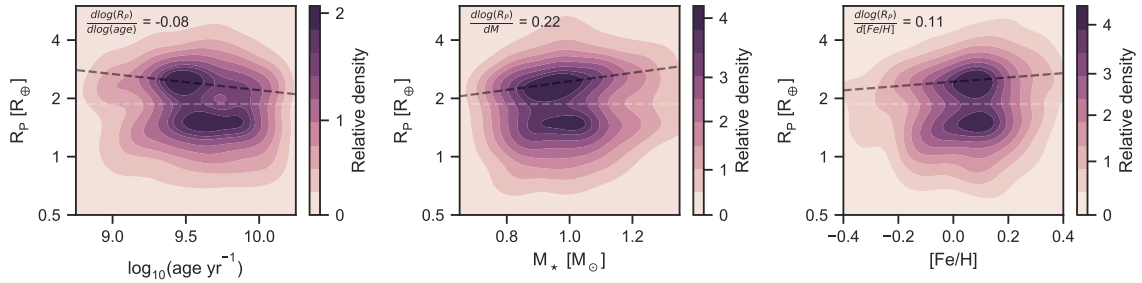


Figure 18. 2D Gaussian kernel density estimates of the distribution of CKS planets in the age-radius (left), stellar mass-radius (middle), and metallicity-radius (right) planes. Our base sample is shown with the additional requirement of fractional radius uncertainties $< 6\%$. The light dashed line indicates the nominal location of the radius valley. The dark dashed lines are not fits but are drawn as a visual guide, with their slopes indicated in the upper left of each panel.

planets in each age bin for bin widths of 0.125, 0.25, 0.5, and 1.0 dex. The results of this analysis are shown in Figure 17. The scarcity of planets with $\log(\text{age}) < 9$ and $\log(\text{age}) > 10$ leads to large uncertainties in the trend at both extremes, in addition to the larger age uncertainties at younger ages. However, we observe a marginally significant increase in the fraction of planets located in the radius valley between $8.75 < \log(\text{age}) < 9.75$. This is in agreement with Figures 2 and 3 which show that the radius valley is weaker among the oldest planets in the CKS sample. Computing planet occurrence rates in the valley as a function of age might lead to a more robust conclusion on the trend noted here, but is outside the scope of the present work.

4. DISCUSSION & CONCLUSIONS

We observe a nearly empty void in the period-radius plane for close-in ($P < 100$ d) exoplanets orbiting stars younger than $\sim 2\text{--}3$ Gyr. The void was first identified among a sample of planets with median posterior isochrone ages < 1.8 Gyr, but is also present among planets with stars rotating faster than an empirical 2.7 Gyr gyrochrone. The

difference between these two timescales could conceivably be due to systematic offsets between the CKS isochrone ages and ages implied from a gyrochronology analysis. Because the gyrochrone used to perform our sample selection is calibrated to open clusters with main-sequence turnoff ages, the longer timescale may more accurately reflect the lifetime of this feature in the period-radius diagram.

We derived an equation for the center of this void, as a function of orbital period, of:

$$\log_{10}(R_P/R_{\oplus}) = -0.08^{(+0.06)}_{(-0.04)} \log_{10}(P/d) + 0.31^{(\pm 0.05)}. \quad (4)$$

As a function of insolation, S_{inc} , the same void is given by the equation,

$$\log_{10}(R_P/R_{\oplus}) = 0.06^{(+0.03)}_{(-0.04)} \log_{10}(S_{\text{inc}}/S_{\oplus}) + 0.13^{(+0.04)}_{(-0.11)}. \quad (5)$$

For periods in the range of 3–30 days, describing the bulk of our sample, this places the center of the radius valley at 1.87–1.56 R_{\oplus} , consistent with previous determinations of the radius valley location. Over this same period range, the lower boundary of the void is in the range of ~ 1.6 –1.4 R_{\oplus} while the upper boundary is at ~ 2.1 –1.8 R_{\oplus} .

The slope of the void in the P-R diagram is consistent at the 1σ level with the slope of the radius valley measured from the asteroseismic sample in V18, but with an intercept that is smaller by $\sim 3\sigma$, using the uncertainty reported by those authors. The smaller intercept among the “young” planet sample corresponds to a shift in the radius valley towards smaller radii, and would be compatible with a prolonged contraction or mass-loss timescale for the most massive sub-Neptunes which have not yet filled in the radius valley.

The shallow, negative slope of the void is compatible with models of atmospheric loss through photoevaporation (e.g. [Owen & Wu 2013, 2017](#); [Lopez & Rice 2018](#); [Jin & Mordasini 2018](#)) or core-cooling ([Gupta & Schlichting 2019, 2020](#)), but incompatible with the steeper negative slope implied for one model of impact-driven atmospheric erosion ([Wyatt et al. 2020](#)). The negative slope we find is also incompatible with the positive slope predicted by models of late stage formation in a gas-poor disk ([Lopez & Rice 2018](#)). However, we note that the void is only marginally inconsistent with being flat when adopting a more conservative regularization parameter in the SVM analysis. The slope of this void in the insolation-radius plane is shallower (by 2–3 σ) than the slope found by [Martinez et al. \(2019\)](#).

Both rotation-selected and isochrone-selected planet samples show the same qualitative trend: a radius valley which is emptier at younger ages and fuller at older ages. We estimate that the probability of this feature being due to chance is $<1\%$, for both the isochrone-selected and rotation-selected samples. We also showed that this feature is relatively insensitive to various data reliability filters and is unlikely to be the result of correlations between stellar age, mass, and metallicity. Simulations accounting for age and planet radius uncertainties show an increasing fraction of planets residing in the valley as a function of age (see Figure 17). The occupancy

of the radius valley is also clearly dependent on the precision of planetary radii and we note that the differences between the young and old planetary samples diminish with more stringent precision requirements (Figure 15). However, resolving the discrepancies entirely requires discarding more than half of the CKS sample. A larger sample size and higher precision planetary radii for the entire CKS sample would help to more securely determine how much of the discrepancy between young and old planet populations is astrophysical and how much is due to noise.

While a more detailed study of planet radius demographics as a function of age, mass, and metallicity is left for future works, we note that our findings are broadly consistent with expectations from both the core-powered mass-loss and photoevaporation theories. This is most evident from Figure 18, where the sub-Neptune size trends with age, mass, and metallicity among those CKS planets with the most precise radii are shown in relation to scalings which approximately, though not exactly, mimic those presented in [Gupta & Schlichting \(2020\)](#). The slope in the stellar mass versus planet radius plane is shallower than predicted in core-cooling models, but more similar to that predicted by photoevaporation models provided that planet mass scales approximately linearly with stellar mass ([Wu 2019](#)). The gigayear timescale we find for evolution of the radius valley is more compatible with core-powered mass-loss models than the canonical timescale of 0.1 Gyr from photoevaporation. However, although photoevaporation models predict the radius gap to emerge on a timescale of 0.1 Gyr, some small fraction of planets are expected to cross the gap on timescales of ~ 1 Gyr or more ([Rogers & Owen 2020](#)), which is compatible with our observations.

The difference in the radius distributions between young and old planets is primarily driven by an absence of large super-Earths ($1.5\text{--}1.8 R_{\oplus}$) at young ages, rather than an absence of small sub-Neptunes. As a result, the peak of the super-Earth radius distribution shifts to larger sizes for older systems. This is an important point in the context of disentangling correlations between stellar mass, age, and metallicity in the CKS sample. The evidence for a wider radius valley among metal-rich stars is driven mostly by larger sub-Neptunes on average, with one explanation being the decreased cooling efficiency of planets with higher metallicity envelopes ([Owen & Murray-Clay 2018](#)). By comparison, we observe a sub-Neptune size distribution which is relatively constant below 3 Gyr while the average size of super-Earths appears to increase over this same time frame (Figure 18). These observations are not easily explained by the anti-correlation between age and [Fe/H] in the CKS sample or the naïve expectation of more massive cores around metal-rich stars from core accretion models. Given that a planet’s size is correlated with its mass, one physical interpretation for this observation is that the largest, most massive cores lose their atmospheres at later times.

It is also worth noting that a prolonged mass-loss timescale for some super-Earths might help to explain the rising occurrence of long-period super-Earths with decreasing metallicity observed by [Owen & Murray-Clay \(2018\)](#). Those authors noted that

such planets are difficult to explain in the photoevaporation model and might have instead formed after the protoplanetary disk dispersed, akin to the canonical view of terrestrial planet formation in the Solar System. However, we note that metallicity and age are correlated in the CKS sample with the median age of the metal-poor sample in [Owen & Murray-Clay \(2018\)](#) being approximately 0.4 dex older than the metal-rich sample. If mass-loss, regardless of the mechanism, proceeds over gigayear timescales then one might expect a rising occurrence of super-Earths with increasing age (and hence decreasing metallicity).

In a companion paper, Sandoval et al. (in prep.) find tentative evidence that the fraction of super-Earths to sub-Neptunes rises with system age from \sim 1–10 Gyr. That work accounts for uncertainties in stellar ages, planetary radii, and the equation for the radius valley itself. That result is in agreement with a similar finding by [Berger et al. \(2020a\)](#) who found, among planets orbiting stars more massive than the Sun, the fraction of super-Earths to sub-Neptunes is higher among older stars (>1 Gyr) than it is for younger stars (<1 Gyr). Collectively, the present work and the studies mentioned above provide evidence for the evolution of small planet radii over gigayear timescales.

The code and data tables required to reproduce the analyses and figures presented in this paper will be made publicly available after submission.

APPENDIX

A. STELLAR AGE VALIDATION

As we are concerned with the time evolution of the exoplanet radius gap, our study hinges on the accuracy of the stellar ages. Main-sequence stars, which constitute the majority of *Kepler* planet hosts, typically have large age uncertainties; this is because the changes in a star’s observable properties over its main sequence lifetime are small relative to typical measurement uncertainties in those properties. However, the high precision of *Gaia* parallaxes and photometry has enabled the determination of relatively *precise* stellar ages from isochrones. The median lower and upper uncertainties on $\log(\text{age})$ for stars in the CKS sample are 0.12 and 0.14 dex, respectively.

A true assessment of the *accuracy* of stellar ages is not possible; essentially all methods for stellar age determination are model-dependent and benchmarks to calibrate these methods are lacking ([Soderblom 2010](#)). However, because the *Kepler* field is so well-studied, it is at least possible to determine the degree of agreement between isochrone ages published by different authors. It is also possible to determine the agreement between ages determined from isochrones versus those determined from gyrochronology or asteroseismology.

To validate the ages used in this study, we compared the isochrone age estimates from F18 with those published in the *Gaia-Kepler* Stellar Properties Catalog (GK-SPC, hereafter B20, [Berger et al. 2020a,b](#)), asteroseismic ages determined in [Silva](#)

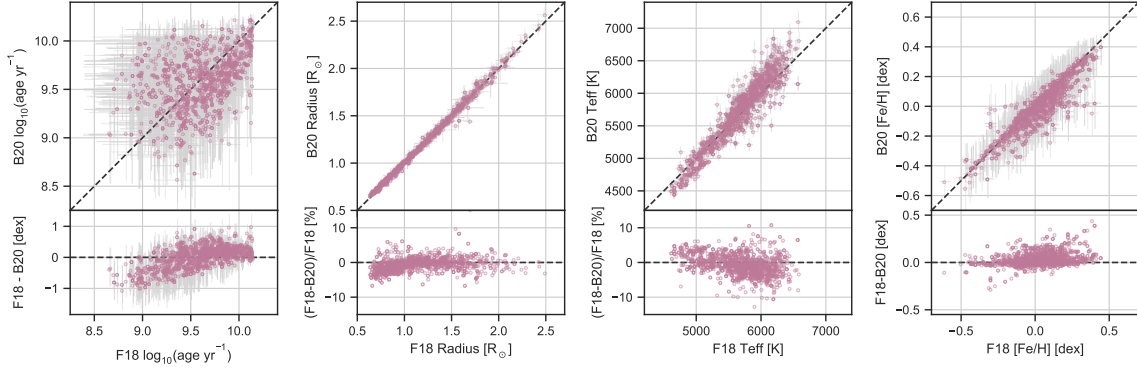


Figure 19. Comparison of F18 and B20 isochrone ages, stellar radii, T_{eff} , and $[\text{Fe}/\text{H}]$ (from left to right). Residuals are shown in the bottom row for each panel.

Aguirre et al. (2015), and with gyrochronology ages determined here. We note that while GKSPC ages exist for a far larger portion of the *Kepler* sample, we restrict our analysis here to only those stars which overlap with CKS VII.

Figure 19 shows the comparison of ages and other parameters from F18 and B20. For 80% of the stars with age estimates in both catalogs, the age estimates agree to within ~ 0.4 dex. The median offset in ages is 0.075 dex, with F18 ages being systematically older, but this shift is smaller than typical age uncertainties from either catalog. The age discrepancies should not be due to differences in the adopted stellar models; both F18 and B20 use the `isoclassify` package (Huber et al. 2017) to compute ages from MIST v1.1 models (Choi et al. 2016; Dotter 2016).

To better understand the origins of the age discrepancies between the two studies, we searched for correlations between $\Delta \log_{10}(\text{age yr}^{-1})$ and other parameters in the dataset. We found that $\Delta \log_{10}(\text{age yr}^{-1})$ is most strongly correlated with ΔM_* and ΔT_{eff} (see Figure 20). As both F18 and B20 determine mass and age simultaneously from stellar models, and these two parameters are intrinsically related, the $\Delta M_* - \Delta \log_{10}(\text{age yr}^{-1})$ correlation is unsurprising. The correlation with ΔT_{eff} , however, is more informative. F18 derived T_{eff} from high-resolution spectroscopy, while B20 derived T_{eff} from isochrones using photometry (specifically Sloan g and 2MASS K_s) and parallaxes as input.

We examined the dependence of T_{eff} -color relations on $[\text{Fe}/\text{H}]$ and A_V and found, when using the CKS spectroscopic parameters, that $[\text{Fe}/\text{H}]$ can explain most of the dispersion in the T_{eff} -color relations. By contrast, when using the photometric T_{eff} and $[\text{Fe}/\text{H}]$ from B20, there is no clear metallicity gradient in the T_{eff} -color relations.

We find that ΔT_{eff} is more strongly correlated with the reddening values (sourced either from B20, L20, or *Gaia*) than it is with any of the metallicity parameters. We conclude that differences in the temperature scales, and hence ages, between the spectroscopic CKS sample (F18) and the photometric GKSPC catalog (B20) may be due to the treatment of reddening.

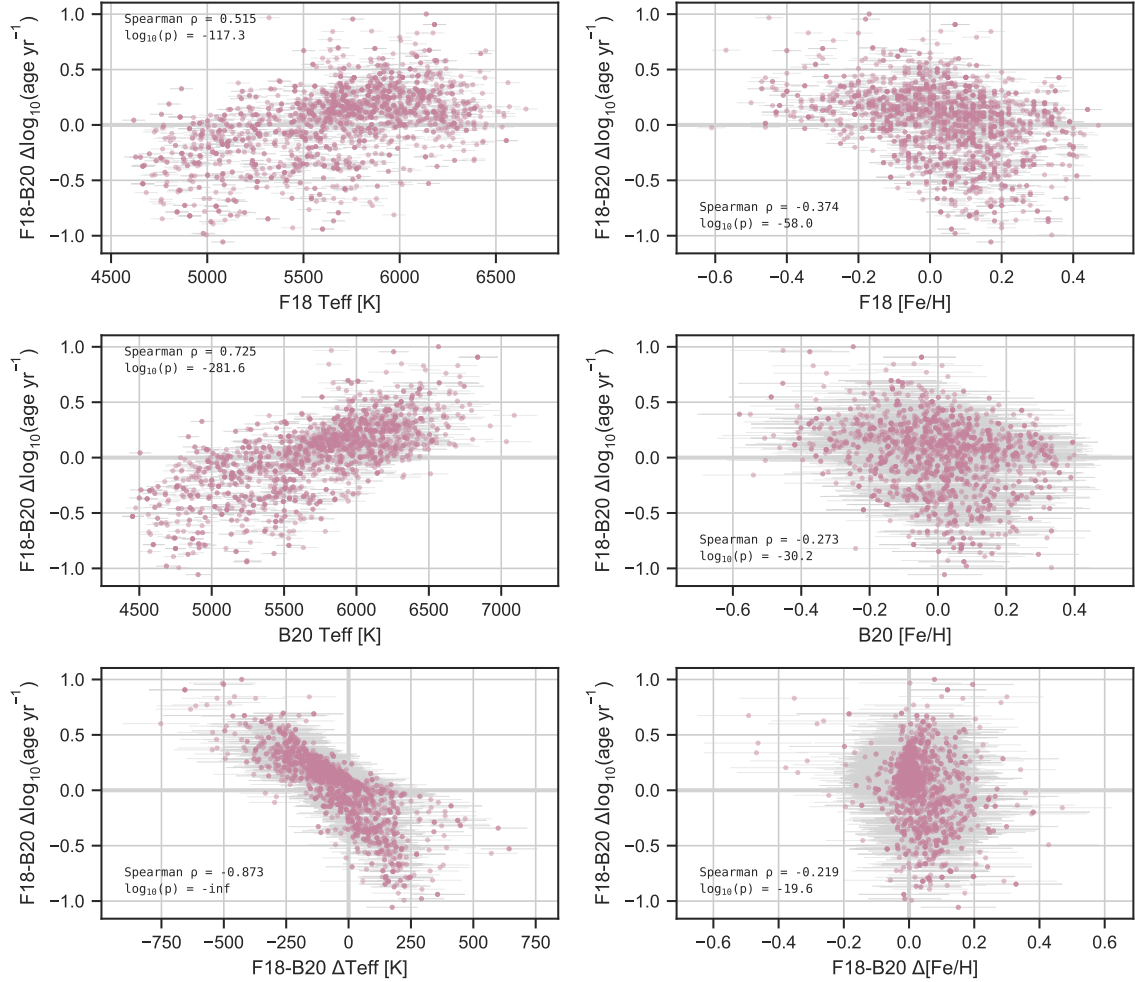


Figure 20. Trends in age discrepancy between the CKS (F18) and GKSPC (B20) catalogs. Errors on the age differences are omitted for clarity.

We next compared the F18 and B20 ages with those determined from precise asteroseismic parameters. Silva Aguirre et al. (2015) determined ages for a sample of 33 *Kepler* planet candidate host stars with high signal-to-noise asteroseismic observations, achieving a median statistical uncertainty of 14% on age. We compare the ages from F18 and B20 with the asteroseismic ages in Figure 21. We find reasonably good agreement with the asteroseismic ages for both F18 and B20. The residual scatter between the isochrone ages and asteroseismic ages is 0.11 dex for F18 and 0.22 dex for B20. In both cases, the residuals are comparable to the median age uncertainties from those catalogs.

Gyrochronology ages were computed using the `stardate` software package (Angus et al. 2019a,b).⁷ The `stardate` ages were computed in the gyrochronology mode alone rather than in the combined isochrone-fitting and gyrochronology mode. The `stardate` gyrochronology relations are calibrated in *Gaia* color space. Using the ro-

⁷ <https://github.com/RuthAngus/stardate>

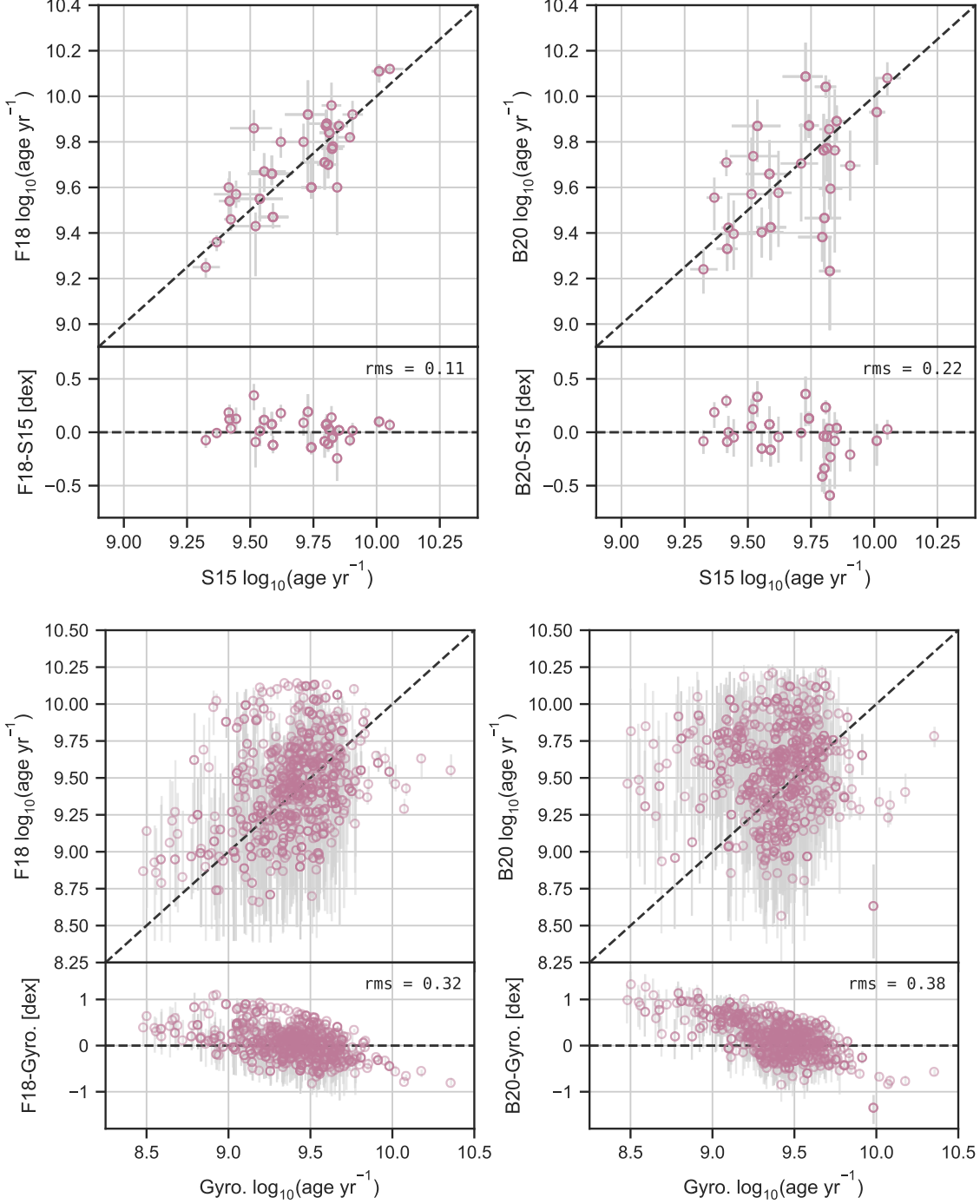


Figure 21. Comparison of F18 and B20 ages with asteroseismic ages from Silva Aguirre et al. (2015) (top panels) and gyrochronology ages from this work.

tation periods we vetted in §2, we noticed increased scatter in the $(B_P - R_P) - P_{\text{rot}}$ plane compared to the $T_{\text{eff}} - P_{\text{rot}}$ plane, where T_{eff} is the CKS spectroscopic temperature from F18. As such, rather than using the star's actual *Gaia* colors which are susceptible to reddening, we converted the F18 spectroscopic T_{eff} to predicted *Gaia* colors using the relation in Curtis et al. (2020) which was calibrated for stars with

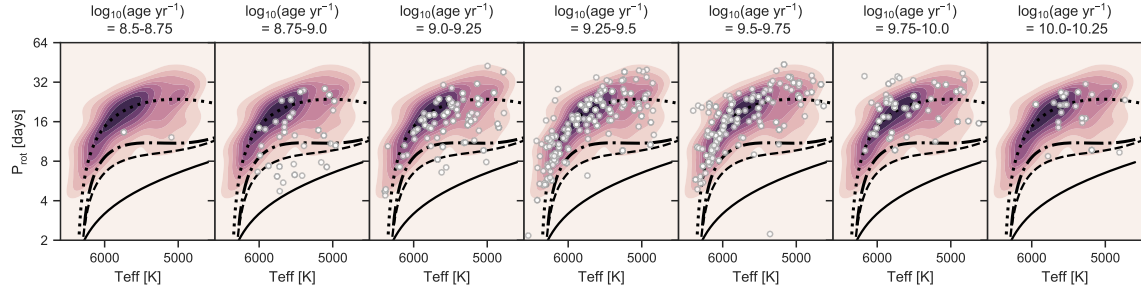


Figure 22. In each panel, contours show the Gaussian kernel density estimate of CKS planet hosts in the $T_{\text{eff}}-P_{\text{rot}}$ plane. Points depict stars with F18 isochrone ages indicated in the titles of each panel. The solid, dashed, dash-dotted, and dotted lines indicate polynomial fits to the empirical gyrochrones of the Pleiades ($\log(\text{age}) \approx 8.1$), Praesepe ($\log(\text{age}) \approx 8.8$), NGC 6811 ($\log(\text{age}) \approx 9$), and NGC 6819 + Ruprecht 147 ($\log(\text{age}) \approx 9.4$) clusters respectively (Curtis et al. 2020).

negligible reddening. Using the vetted P_{rot} and predicted $(B_P - R_P)$ colors we then computed the gyrochronology ages (without uncertainties). Our comparison of the isochrone ages and gyrochronology ages is shown in Figure 21, indicating comparable scatter for F18 and B20. However, we note that there is better agreement between F18 and the gyrochronology ages at young ages (<1 Gyr).

We note that the `stardate` model has not been updated to include recently-determined open cluster rotation period sequences in its calibration. As such, we can compare the CKS sample to empirical gyrochrones from Curtis et al. (2020). This comparison is shown in Figure 22, which shows that the F18 isochrone ages do not always map predictably onto the $T_{\text{eff}}-P_{\text{rot}}$ plane. For example, in the F18 $\log(\text{age})$ bin of 8.75-9 dex, approximately half of the stars fall below the 1 Gyr gyrochrones and half lie above it. Similarly, in the F18 $\log(\text{age})$ bin of 9.5-9.75 dex, a non-negligible number of stars fall below the $\log(\text{age}) \approx 9.4$ gyrochrones. However, we note that the vast majority of stars with F18 isochrone ages of $\log(\text{age}) < 9.25$ fall below the $\log(\text{age}) \approx 9.4$ gyrochrones. This is in agreement with the comparison made to the `stardate` gyrochronology ages, in the sense that the majority of stars with F18 isochrone ages $\lesssim 1.8$ Gyr appear to be younger than $\lesssim 2.7$ Gyr from a gyrochronology analysis.

Finally, we also examined the evolution of other physical parameters known to correlate with age, such as the variability amplitude R_{var} , NUV excess, and the velocity dispersion. We tracked velocity dispersion using v_{tan} , the velocity tangential to the celestial sphere, and v_b , the velocity in the direction of the galactic latitude, sourced from Lu et al. (2020). *GALEX* NUV magnitudes were obtained from Olmedo et al. (2015). For a crude approximation of the NUV excess, we performed a quadratic fit to the full *Kepler* Q1-Q17 DR25 sample in the $(G - G_{RP})$ vs. $(NUV - K_s)$ color-color diagram. The NUV excess was then defined as a star's $(NUV - K_s)$ color minus the quadratic color-color trend. No de-reddening was performed. Figure 23 shows the evolution of these parameters as a function of age. For both the F18 and B20

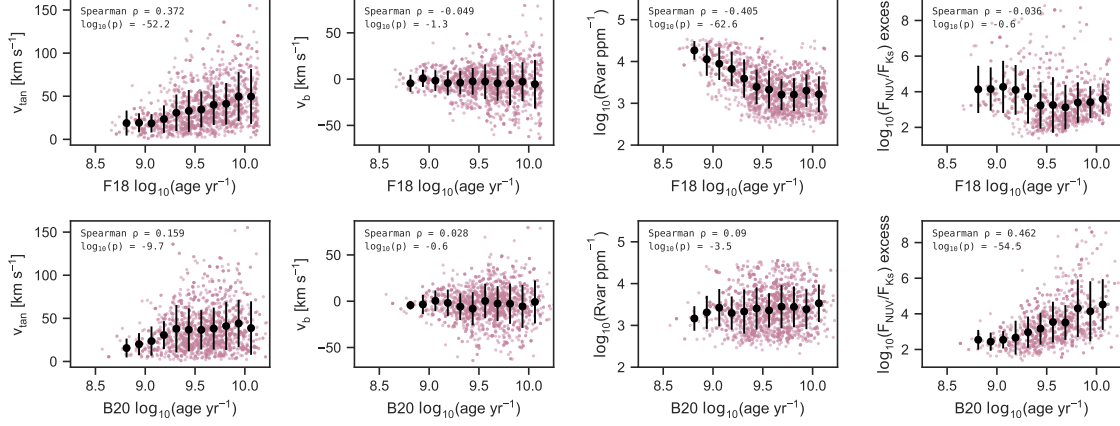


Figure 23. Validation of isochronal age estimates. The v_{\tan} and v_b velocities (left and middle columns) and R_{var} as a function of isochronal ages from F18 (top row) and B20 (bottom row). Spearman rank correlation coefficients (ρ) and p-values are printed in the top left corner of each panel. Black points with errorbars indicate the mean and standard deviation of the data binned by 0.125 dex in $\log(\text{age})$.

isochrone ages, we observe increasing dispersion in v_{\tan} and v_b with age, as expected. The strongest expected correlation is observed for R_{var} (sourced from Lu et al. 2020) and F18 age, with R_{var} declining for the first ~ 3 Gyr before plateauing. The average NUV excess appears to decline over a similar timescale when using the F18 ages, though that trend is less significant and there may be residual systematics from the manner in which we computed the excess. Both the R_{var} and NUV excess trends are expected, as starspot coverage, variability amplitudes, and chromospheric activity are known to decline with age. By comparison, when using the B20 ages the behavior of R_{var} and NUV excess with age is not as expected. We conclude by noting that, while substantial uncertainties remain for isochronal ages, there is qualitative agreement between the CKS ages and ages (or age indicators) derived from independent methods. In some of the comparisons above the CKS and GKSPC ages perform comparably well, though it is at the youngest ages ($\lesssim 3$ Gyr) where the GKSPC ages do not reproduce some expected trends. As the evolution of *Kepler* planets at early times is a primary focus of this work, we adopt the CKS ages.

ACKNOWLEDGMENTS

We thank Eric Ford, Christina Hedges, David W. Hogg, and Josh Winn for helpful discussions. TJD is grateful to Chelsea Yarnell for her irreplaceable support throughout the COVID-19 pandemic. This paper includes data collected by the *Kepler* mission, funded by the NASA Science Mission directorate. This work presents results from the European Space Agency (ESA) space mission Gaia. Gaia data are being processed by the Gaia Data Processing and Analysis Consortium (DPAC). Funding for the DPAC is provided by national institutions, in particular the institutions participating in the Gaia MultiLateral Agreement (MLA). The Gaia mission website is <https://www.cosmos.esa.int/gaia>. The Gaia archive website is <https://archives.esac.esa.int/gaia>. This work made use of the gaia-kepler.fun cross-match database created by Megan Bedell.

Facilities: Kepler; Gaia; GALEX

Software: `astropy` (Astropy Collaboration et al. 2013, 2018), `jupyter` (Kluyver et al. 2016), `matplotlib` (Hunter 2007), `numpy` (van der Walt et al. 2011), `pandas` (pandas development team 2020; Wes McKinney 2010), `seaborn` (Waskom et al. 2017), `scikit-learn` (Pedregosa et al. 2011) `scipy` (Jones et al. 2001–)

REFERENCES

Akeson, R. L., Chen, X., Ciardi, D., et al. 2013, PASP, 125, 989, doi: [10.1086/672273](https://doi.org/10.1086/672273)

Angus, R., Morton, T., Aigrain, S., Foreman-Mackey, D., & Rajpaul, V. 2018, MNRAS, 474, 2094, doi: [10.1093/mnras/stx2109](https://doi.org/10.1093/mnras/stx2109)

Angus, R., Morton, T., & Foreman-Mackey, D. 2019a, The Journal of Open Source Software, 4, 1469, doi: [10.21105/joss.01469](https://doi.org/10.21105/joss.01469)

Angus, R., Morton, T. D., Foreman-Mackey, D., et al. 2019b, AJ, 158, 173, doi: [10.3847/1538-3881/ab3c53](https://doi.org/10.3847/1538-3881/ab3c53)

Astropy Collaboration, Robitaille, T. P., Tollerud, E. J., et al. 2013, A&A, 558, A33, doi: [10.1051/0004-6361/201322068](https://doi.org/10.1051/0004-6361/201322068)

Astropy Collaboration, Price-Whelan, A. M., SipH ocz, B. M., et al. 2018, AJ, 156, 123, doi: [10.3847/1538-3881/aabc4f](https://doi.org/10.3847/1538-3881/aabc4f)

Belokurov, V., Penoyre, Z., Oh, S., et al. 2020, MNRAS, 496, 1922, doi: [10.1093/mnras/staa1522](https://doi.org/10.1093/mnras/staa1522)

Berger, T. A., Huber, D., Gaidos, E., van Saders, J. L., & Weiss, L. M. 2020a, arXiv e-prints, arXiv:2005.14671, <https://arxiv.org/abs/2005.14671>

Berger, T. A., Huber, D., van Saders, J. L., et al. 2020b, AJ, 159, 280, doi: [10.3847/1538-3881/159/6/280](https://doi.org/10.3847/1538-3881/159/6/280)

Borucki, W. J., Koch, D., Basri, G., et al. 2010, Science, 327, 977, doi: [10.1126/science.1185402](https://doi.org/10.1126/science.1185402)

Burke, C. J., Christiansen, J. L., Mullally, F., et al. 2015, ApJ, 809, 8, doi: [10.1088/0004-637X/809/1/8](https://doi.org/10.1088/0004-637X/809/1/8)

Carter, J. A., Agol, E., Chaplin, W. J., et al. 2012, Science, 337, 556, doi: [10.1126/science.1223269](https://doi.org/10.1126/science.1223269)

Chatterjee, S., & Chen, H. 2018, ApJ, 852, 58, doi: [10.3847/1538-4357/aa9e05](https://doi.org/10.3847/1538-4357/aa9e05)

Chen, H., & Rogers, L. A. 2016, ApJ, 831, 180, doi: [10.3847/0004-637X/831/2/180](https://doi.org/10.3847/0004-637X/831/2/180)

Choi, J., Dotter, A., Conroy, C., et al. 2016, *ApJ*, 823, 102, doi: [10.3847/0004-637X/823/2/102](https://doi.org/10.3847/0004-637X/823/2/102)

Cloutier, R., & Menou, K. 2020, *AJ*, 159, 211, doi: [10.3847/1538-3881/ab8237](https://doi.org/10.3847/1538-3881/ab8237)

Curtis, J. L., Agüeros, M. A., Matt, S. P., et al. 2020, arXiv e-prints, arXiv:2010.02272. <https://arxiv.org/abs/2010.02272>

Cutri, R. M., Skrutskie, M. F., van Dyk, S., et al. 2003, 2MASS All Sky Catalog of point sources.

Dong, S., Xie, J.-W., Zhou, J.-L., Zheng, Z., & Luo, A. 2018, *Proceedings of the National Academy of Science*, 115, 266, doi: [10.1073/pnas.1711406115](https://doi.org/10.1073/pnas.1711406115)

Dotter, A. 2016, *ApJS*, 222, 8, doi: [10.3847/0067-0049/222/1/8](https://doi.org/10.3847/0067-0049/222/1/8)

Fressin, F., Torres, G., Charbonneau, D., et al. 2013, *ApJ*, 766, 81, doi: [10.1088/0004-637X/766/2/81](https://doi.org/10.1088/0004-637X/766/2/81)

Fulton, B. J., & Petigura, E. A. 2018, *AJ*, 156, 264, doi: [10.3847/1538-3881/aae828](https://doi.org/10.3847/1538-3881/aae828)

Fulton, B. J., Petigura, E. A., Howard, A. W., et al. 2017, *AJ*, 154, 109, doi: [10.3847/1538-3881/aa80eb](https://doi.org/10.3847/1538-3881/aa80eb)

Furlan, E., Ciardi, D. R., Everett, M. E., et al. 2017, *AJ*, 153, 71, doi: [10.3847/1538-3881/153/2/71](https://doi.org/10.3847/1538-3881/153/2/71)

Gaia Collaboration, Brown, A. G. A., Vallenari, A., et al. 2018, *A&A*, 616, A1, doi: [10.1051/0004-6361/201833051](https://doi.org/10.1051/0004-6361/201833051)

Ginzburg, S., Schlichting, H. E., & Sari, R. 2016, *ApJ*, 825, 29, doi: [10.3847/0004-637X/825/1/29](https://doi.org/10.3847/0004-637X/825/1/29)

—. 2018, *MNRAS*, 476, 759, doi: [10.1093/mnras/sty290](https://doi.org/10.1093/mnras/sty290)

Gupta, A., & Schlichting, H. E. 2019, *MNRAS*, 487, 24, doi: [10.1093/mnras/stz1230](https://doi.org/10.1093/mnras/stz1230)

—. 2020, *MNRAS*, 493, 792, doi: [10.1093/mnras/staa315](https://doi.org/10.1093/mnras/staa315)

Hansen, J. T., Casagrande, L., Ireland, M. J., & Lin, J. 2020, arXiv e-prints, arXiv:2009.08154. <https://arxiv.org/abs/2009.08154>

Huber, D., Zinn, J., Bojsen-Hansen, M., et al. 2017, *ApJ*, 844, 102, doi: [10.3847/1538-4357/aa75ca](https://doi.org/10.3847/1538-4357/aa75ca)

Hunter, J. D. 2007, *Computing in Science and Engineering*, 9, 90, doi: [10.1109/MCSE.2007.55](https://doi.org/10.1109/MCSE.2007.55)

Inamdar, N. K., & Schlichting, H. E. 2016, *ApJL*, 817, L13, doi: [10.3847/2041-8205/817/2/L13](https://doi.org/10.3847/2041-8205/817/2/L13)

Jackson, A. P., Davis, T. A., & Wheatley, P. J. 2012, *MNRAS*, 422, 2024, doi: [10.1111/j.1365-2966.2012.20657.x](https://doi.org/10.1111/j.1365-2966.2012.20657.x)

Jin, S., & Mordasini, C. 2018, *ApJ*, 853, 163, doi: [10.3847/1538-4357/aa9f1e](https://doi.org/10.3847/1538-4357/aa9f1e)

Jin, S., Mordasini, C., Parmentier, V., et al. 2014, *ApJ*, 795, 65, doi: [10.1088/0004-637X/795/1/65](https://doi.org/10.1088/0004-637X/795/1/65)

Johnson, J. A., Petigura, E. A., Fulton, B. J., et al. 2017, *AJ*, 154, 108, doi: [10.3847/1538-3881/aa80e7](https://doi.org/10.3847/1538-3881/aa80e7)

Jones, E., Oliphant, T., Peterson, P., et al. 2001–, SciPy: Open source scientific tools for Python. <http://www.scipy.org/>

King, G. W., & Wheatley, P. J. 2020, arXiv e-prints, arXiv:2007.13731. <https://arxiv.org/abs/2007.13731>

Kluyver, T., Ragan-Kelley, B., Pérez, F., et al. 2016, in *Positioning and Power in Academic Publishing: Players, Agents and Agendas*, ed. F. Loizides & B. Schmidt, IOS Press, 87 – 90

Lee, E. J., & Chiang, E. 2016, *ApJ*, 817, 90, doi: [10.3847/0004-637X/817/2/90](https://doi.org/10.3847/0004-637X/817/2/90)

Lee, E. J., Chiang, E., & Ormel, C. W. 2014, *ApJ*, 797, 95, doi: [10.1088/0004-637X/797/2/95](https://doi.org/10.1088/0004-637X/797/2/95)

Lindgren, L., Hernández, J., Bombrun, A., et al. 2018, *A&A*, 616, A2, doi: [10.1051/0004-6361/201832727](https://doi.org/10.1051/0004-6361/201832727)

Liu, S.-F., Hori, Y., Lin, D. N. C., & Asphaug, E. 2015, *ApJ*, 812, 164, doi: [10.1088/0004-637X/812/2/164](https://doi.org/10.1088/0004-637X/812/2/164)

Lopez, E. D., & Fortney, J. J. 2013, *ApJ*, 776, 2, doi: [10.1088/0004-637X/776/1/2](https://doi.org/10.1088/0004-637X/776/1/2)

Lopez, E. D., Fortney, J. J., & Miller, N. 2012, *ApJ*, 761, 59, doi: [10.1088/0004-637X/761/1/59](https://doi.org/10.1088/0004-637X/761/1/59)

Lopez, E. D., & Rice, K. 2018, *MNRAS*, 479, 5303, doi: [10.1093/mnras/sty1707](https://doi.org/10.1093/mnras/sty1707)

Lu, Y., Angus, R., Agüeros, M. A., et al. 2020, arXiv e-prints, arXiv:2008.03351. <https://arxiv.org/abs/2008.03351>

Martinez, C. F., Cunha, K., Ghezzi, L., & Smith, V. V. 2019, *ApJ*, 875, 29, doi: [10.3847/1538-4357/ab0d93](https://doi.org/10.3847/1538-4357/ab0d93)

Mazeh, T., Perets, H. B., McQuillan, A., & Goldstein, E. S. 2015, *ApJ*, 801, 3, doi: [10.1088/0004-637X/801/1/3](https://doi.org/10.1088/0004-637X/801/1/3)

McQuillan, A., Mazeh, T., & Aigrain, S. 2013, *ApJL*, 775, L11, doi: [10.1088/2041-8205/775/1/L11](https://doi.org/10.1088/2041-8205/775/1/L11)

Morton, T. D., Bryson, S. T., Coughlin, J. L., et al. 2016, *ApJ*, 822, 86, doi: [10.3847/0004-637X/822/2/86](https://doi.org/10.3847/0004-637X/822/2/86)

Mullally, F., Coughlin, J. L., Thompson, S. E., et al. 2015, *ApJS*, 217, 31, doi: [10.1088/0067-0049/217/2/31](https://doi.org/10.1088/0067-0049/217/2/31)

Olmedo, M., Lloyd, J., Mamajek, E. E., et al. 2015, *ApJ*, 813, 100, doi: [10.1088/0004-637X/813/2/100](https://doi.org/10.1088/0004-637X/813/2/100)

Owen, J. E., & Jackson, A. P. 2012, *MNRAS*, 425, 2931, doi: [10.1111/j.1365-2966.2012.21481.x](https://doi.org/10.1111/j.1365-2966.2012.21481.x)

Owen, J. E., & Morton, T. D. 2016, *ApJL*, 819, L10, doi: [10.3847/2041-8205/819/1/L10](https://doi.org/10.3847/2041-8205/819/1/L10)

Owen, J. E., & Murray-Clay, R. 2018, *MNRAS*, 480, 2206, doi: [10.1093/mnras/sty1943](https://doi.org/10.1093/mnras/sty1943)

Owen, J. E., & Wu, Y. 2013, *ApJ*, 775, 105, doi: [10.1088/0004-637X/775/2/105](https://doi.org/10.1088/0004-637X/775/2/105)

—. 2017, *ApJ*, 847, 29, doi: [10.3847/1538-4357/aa890a](https://doi.org/10.3847/1538-4357/aa890a)

pandas development team, T. 2020, *pandas-dev/pandas: Pandas, latest, Zenodo*, doi: [10.5281/zenodo.3509134](https://doi.org/10.5281/zenodo.3509134)

Pedregosa, F., Varoquaux, G., Gramfort, A., et al. 2011, *Journal of Machine Learning Research*, 12, 2825

Petigura, E. A. 2020, *AJ*, 160, 89, doi: [10.3847/1538-3881/ab9fff](https://doi.org/10.3847/1538-3881/ab9fff)

Petigura, E. A., Howard, A. W., & Marcy, G. W. 2013, *Proceedings of the National Academy of Science*, 110, 19273, doi: [10.1073/pnas.1319909110](https://doi.org/10.1073/pnas.1319909110)

Petigura, E. A., Howard, A. W., Marcy, G. W., et al. 2017, *AJ*, 154, 107, doi: [10.3847/1538-3881/aa80de](https://doi.org/10.3847/1538-3881/aa80de)

Petigura, E. A., Marcy, G. W., Winn, J. N., et al. 2018, *AJ*, 155, 89, doi: [10.3847/1538-3881/aaa54c](https://doi.org/10.3847/1538-3881/aaa54c)

Rogers, J. G., & Owen, J. E. 2020, *arXiv e-prints*, arXiv:2007.11006. <https://arxiv.org/abs/2007.11006>

Rogers, L. A. 2015, *ApJ*, 801, 41, doi: [10.1088/0004-637X/801/1/41](https://doi.org/10.1088/0004-637X/801/1/41)

Sanchis-Ojeda, R., Rappaport, S., Winn, J. N., et al. 2014, *ApJ*, 787, 47, doi: [10.1088/0004-637X/787/1/47](https://doi.org/10.1088/0004-637X/787/1/47)

Silva Aguirre, V., Davies, G. R., Basu, S., et al. 2015, *MNRAS*, 452, 2127, doi: [10.1093/mnras/stv1388](https://doi.org/10.1093/mnras/stv1388)

Smith, J. C., Stumpe, M. C., Van Cleve, J. E., et al. 2012, *PASP*, 124, 1000, doi: [10.1086/667697](https://doi.org/10.1086/667697)

Soderblom, D. R. 2010, *ARA&A*, 48, 581, doi: [10.1146/annurev-astro-081309-130806](https://doi.org/10.1146/annurev-astro-081309-130806)

Stumpe, M. C., Smith, J. C., Van Cleve, J. E., et al. 2012, *PASP*, 124, 985, doi: [10.1086/667698](https://doi.org/10.1086/667698)

Tu, L., Johnstone, C. P., Güdel, M., & Lammer, H. 2015, *A&A*, 577, L3, doi: [10.1051/0004-6361/201526146](https://doi.org/10.1051/0004-6361/201526146)

van der Walt, S., Colbert, S. C., & Varoquaux, G. 2011, *Computing in Science and Engineering*, 13, 22, doi: [10.1109/MCSE.2011.37](https://doi.org/10.1109/MCSE.2011.37)

Van Eylen, V., Agentoft, C., Lundkvist, M. S., et al. 2018, *MNRAS*, 479, 4786, doi: [10.1093/mnras/sty1783](https://doi.org/10.1093/mnras/sty1783)

Walkowicz, L. M., & Basri, G. S. 2013, *MNRAS*, 436, 1883, doi: [10.1093/mnras/stt1700](https://doi.org/10.1093/mnras/stt1700)

Waskom, M., Botvinnik, O., O’Kane, D., et al. 2017, *mwaskom/seaborn: v0.8.1 (September 2017)*, v0.8.1, Zenodo, doi: [10.5281/zenodo.883859](https://doi.org/10.5281/zenodo.883859)

Weiss, L. M., & Marcy, G. W. 2014, *ApJL*, 783, L6, doi: [10.1088/2041-8205/783/1/L6](https://doi.org/10.1088/2041-8205/783/1/L6)

Wes McKinney. 2010, in *Proceedings of the 9th Python in Science Conference*, ed. Stéfan van der Walt & Jarrod Millman, 56 – 61, doi: [10.25080/Majora-92bf1922-00a](https://doi.org/10.25080/Majora-92bf1922-00a)

Wu, Y. 2019, *ApJ*, 874, 91, doi: [10.3847/1538-4357/ab06f8](https://doi.org/10.3847/1538-4357/ab06f8)

Wyatt, M. C., Kral, Q., & Sinclair, C. A. 2020, *MNRAS*, 491, 782, doi: [10.1093/mnras/stz3052](https://doi.org/10.1093/mnras/stz3052)

Zhu, W., Petrovich, C., Wu, Y., Dong, S.,
& Xie, J. 2018, ApJ, 860, 101,
doi: [10.3847/1538-4357/aac6d5](https://doi.org/10.3847/1538-4357/aac6d5)